MICROBOONE-NOTE-1017-PUB v1.0

A Method to Extract the Charge Distribution Arriving at the TPC Wire Planes in MicroBooNE

The MicroBooNE Collaboration

(Dated: June 29, 2016)

In this technote, we describe the concept and general strategy of LArTPC drifted-charge extraction, which converts the raw digitized TPC waveform to the number of ionized electrons passing through the wire plane at a given time. The proper recovery of the number of ionized electrons from all wire planes is important to the success of the subsequent reconstruction algorithms. A number of building blocks for the processing algorithm are described and characterized.

An example of implementation of the algorithm was realized inside the Wire-Cell reconstruction package. The performance was qualitatively illustrated on MicroBooNE data with event display pictures, which shows significant improvements. Some metrics to evaluate the performance of the TPC signal extraction procedure are described. Next steps towards the quantification of the effect of the proposed concept and optimization of the procedure are outlined.

CONTENTS

1. OVERVIEW OF LARTPC SIGNAL FORMATION

The Liquid Argon Time Projection Chamber (LArTPC) [1–4] is a novel detector being developed worldwide for neutrino experiments. The MicroBooNE experiment [5, 6] is the first experiment in the US using a 100-ton scale single-phase LArTPC to detect accelerator neutrinos.

The principle of the single-phase LArTPC with wire readouts is shown in Fig. 1. When charged particles traverse the LAr medium, ionization electrons are generated. They travel at a constant speed (∼1.6 mm/μs at 500 V/cm electric field) along the external electric field toward the multiple anode wire planes. The early wire planes collect induction signals as the drifting electrons pass through. The electrons are collected on the wires in the final plane. The transparency of the induction planes is assured by applying appropriate bias voltages to these wire planes. During this process, currents are produced on the wire planes. Since the locations of wires are accurately known, the positions of the ionization electrons in the direction perpendicular to the drift can be determined in multiple independent wire-plane views. The time of the initial interaction can be determined by collecting scintillation light in a fast optical detector system. By measuring the time from this prompt activity to signals on the wires, the longitudinal position along the drift direction can be determined. Therefore, a 3D imaging of the trajectories of the charged particles in the LAr can be achieved. The number of ionization electrons along the particle trajectories depends on the energy and type of the particles, and can be used to deduce their properties.

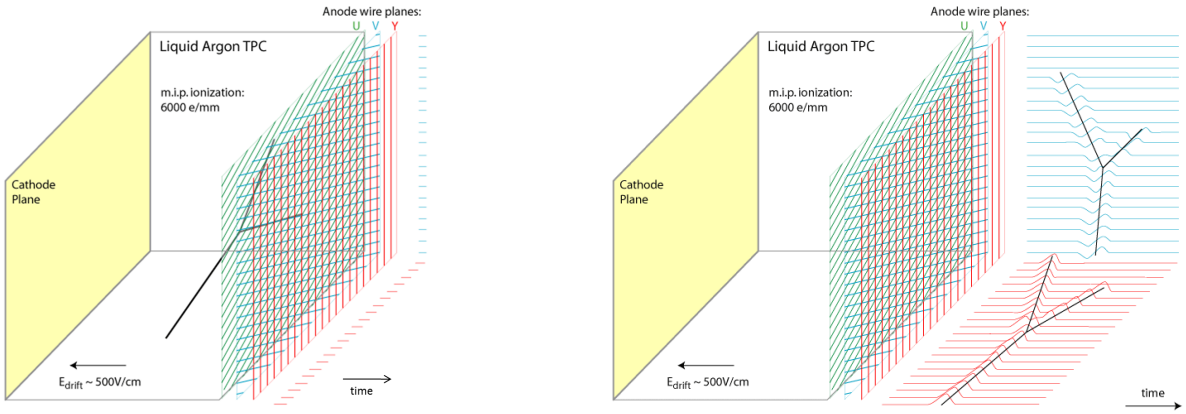

FIG. 1. The principle of LArTPC is shown. (left) When energetic, charged particles traverse the LAr medium, ionization electrons are produced and move along the external electric field towards the anode planes. (right) The ionization electrons pass through the induction wire planes and are collected by the final collection wire plane. During this process, signals are measured on the wires in each plane which provides information about the 3D positions and energies of initial particles.

Figure 2 illustrates the major elements of the processes involved in forming the TPC signals. When the ionization electrons drift through the wire planes, current is induced on the nearby wires. This process is described by the *field response functions*. The principle of the current induction is described by the Shockley-Ramo theorem [7, 8]. For an element of ionization charge, the instantaneous induced current i is proportional to the amount of that charge q:

$$i = q \cdot \vec{E}_w \cdot \vec{v}_q. \tag{1}$$

The proportionality factor is product of the weighting field vector $\vec{E}_w$ at the location of the charge and its drifting velocity vector $\vec{v}_q$. The weighting field vector $\vec{E}_w$, which depends on the geometry of the electrodes, can be calculated by removing the charge, placing the potential of the targeted electrode to the unity potential, and setting all other conductors to ground. Figure 2 shows a calculated weighting potential for one induction plane wire using a 2D simulation based on Garfield [9]. The simulation assumes MicroBooNE geometry; the wire pitch is 3 mm. There are three wire planes, with the first two being induction and last one being collection plane. The drifting velocity $\vec{v}_q$ is a function of the external electric field, which also depends on the geometry of the electrodes as well as the applied drifting and bias voltages.

The induced current on the wire is received, amplified, and shaped by a pre-amplifier. This process is described by the *electronics response function*. The resulting signal waveform is then digitally sampled at regular intervals. The *raw digit* is defined as the collection of samples of charge vs. time for a single channel. The goal of the drifted-charge extraction process is to use the measured raw digits to restore the number of ionization electrons that have arrived at each anode plane at a given sampling time. The information regarding the amount, wire location, and arriving time of ionization electrons are then used as input to the later event reconstruction chain.

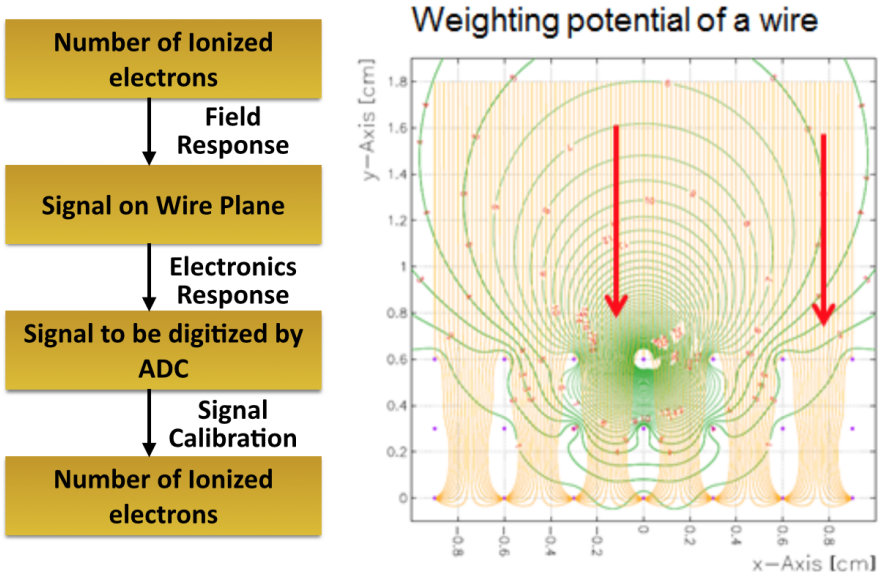

FIG. 2. An illustration of the process of TPC signal formation. See text for more explanations.

While the principle is straightforward, the induction current itself can be rather complicated. As shown in Fig. 2, the weighting field becomes smaller at locations further away from the wire of interest. The weighting field also extends beyond the "boundary" of the wire. The boundaries associated with a wire are defined by two imaginary planes parallel to a wire, and half way between two neighboring wires. That is, within an ideal case, all charges produced inside the boundary will drift to its associated wire (we will refer this region as the *wire region*). Due to the extent of the weighting field, electrons drifting inside a wire region can induce current in other wires. This fact makes the induced current strongly depend on the local ionization charge distribution near the wire of interest, which in turn depends on the topology of the initial particles.

Figure 3 shows an example of the simulated (left) and measured (right) TPC signals on the first wire plane (U-plane) in MicroBooNE. The left panel shows the cumulative contribution from the ionization charge drifting within the wire region of interest from an ideal track with uniform charge distribution traveling parallel to the wire plane. Also shown are the contributions from the ionization charged passing through the neighboring wire regions on either side for this parallel track. It is clear that the positive half of the signal, which is formed when the ionization electrons are moving toward the wire, is significantly altered by the local ionization charge distribution. The right panel shows the measured TPC signal for tracks traveling at different angles with respect to the wire plane. The 0 degree direction is perpendicular to the electric field and thus parallel to the wire plane. Conversely tracks going in the 90 degree direction travel parallel to the electric field and thus perpendicular to the wire plane. These signals are plotted normalized according to their peak heights on the negative half of the signal. This peak corresponds to the ionization electrons moving away from the wire plane. Since the absolute amount of ionization charge is not precisely known, the scale of the Y-axis is taken as arbitrary. It is clear that the average TPC response function strongly depends on the track angle. Again, this shows a dependency on the local ionization charge distribution and is qualitatively consistent with the expectation from the simulation. We should also note that the coherent noise removal procedure described in Ref. [10] also leads to distortions of the average field response function, especially for tracks traveling close to 0 degrees.

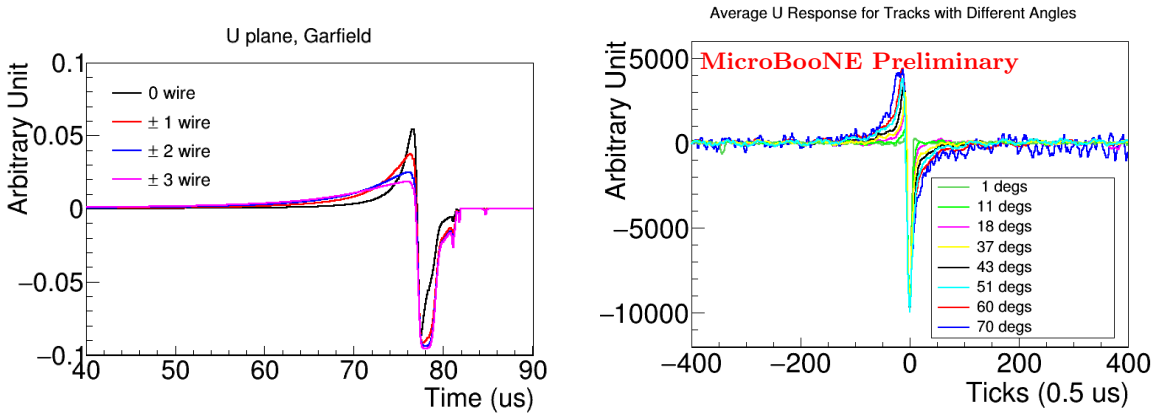

FIG. 3. (left) Simulated TPC signals for a track traveling parallel to the wire plane. The response of charge drifting within a wire region (0 wire) and the response including charge drifting in the three neighboring wire regions on either side are shown. (right) Measured TPC signals for tracks traveling at different angles with respect to the wire plane. See text for more discussion.

2. TPC DRIFTED-CHARGE EXTRACTION

2.1. Overview

As shown in Fig. 2, the goal of TPC drifted-charge profiling is to restore the number of ionized electrons at a given sampling time from the digitized TPC signal. In this section, we describe the concepts for the various required techniques and their software implementation.

2.2. Deconvolution Technique

The deconvolution technique was introduced to LArTPC signal processing by Bruce Baller in the context Argoneut data analysis [11]. The goal of the deconvolution is to "remove" the impact of field and electronics responses from the measured signal to recover the number of ionized electrons. This technique has the advantages of being robust and fast and is an essential step in the overall drifted-charge profiling process.

Deconvolution is a mathematical technique to extract a *real signal* $S(t)$ from a *measured signal* $M(t_0)$. The measured signal is modeled as a convolution integral over the real signal $S(t)$ and a given detector *response function* $R(t, t_0)$ which gives the instantaneous portion of the measured signal at some time t_0 due to an element of real signal at time t:

$$M(t_0) = \int_{-\infty}^{\infty} R(t, t_0) \cdot S(t) \cdot dt. \tag{2}$$

If the detector response function only depends on the relative time difference between t and t_0,

$$R(t, t_0) \equiv R(t - t_0), \tag{3}$$

we can solve the above equation by doing a Fourier transformation on both sides of the equation:

$$M(\omega) = R(\omega) \cdot S(\omega), \tag{4}$$

where ω is the frequency. In this case, we can derive the signal in the frequency domain by taking the ratio of measured signal and the given response function:

$$S(\omega) = \frac{M(\omega)}{R(\omega)}. \tag{5}$$

The real signal in the time domain can then be obtained by applying the inverse Fourier transformation from the frequency domain.

The Shockley-Ramo response function $R(\omega)$ does not address contributions to the measured signal which are due to real world sources of electrical *noise* from thermal and unwanted transmitting sources or the

approximation in the digitization. Such contributions to $M(\omega)$ will not be removed by the deconvolution. Worse, because the response function becomes small (see below) at low frequencies for the induction planes and at high frequencies for all planes, the noise components in these frequencies will be enhanced by the deconvolution.

To address the issue of noise, a *filter function* $F(\omega)$ is introduced. Its purpose is to attenuate the problematic noise. The addition of this function can be considered an augmentation to the response function. The two functions are kept distinct for clarity in the notation here. Equation (5) is then updated to become

$$S(\omega) = \frac{M(\omega)}{R(\omega)} \cdot F(\omega). \tag{6}$$

With a suitable noise filtering model an improved estimator for the signal $S(t)$ in the time domain can then be found by applying an inverse Fourier transform to $S(\omega)$. Essentially, the deconvolution replaces the real field and electronics response function with an effective software filter response function. The advantage of this procedure is more pronounced on the induction plane where the irregular bipolar field response function is replaced by a regular uni-polar response function through the inclusion of the software filter.

2.3. Nature of Deconvolution and Role of Software Filter

In the previous section, we described the basic procedure of the signal deconvolution through forward and inverse Fourier transforms. In practice, the measured signal is digitally sampled at a fixed frequency. In this case the deconvolution employs forward and inverse Discrete Fourier Transformations (DFT). In this section we describe the deconvolution formalism in terms of DFT and χ^2 minimization and the role of the filter function.

2.3.1. Signal Extraction with Matrix Inversion

First, let's examine the problem in the time domain before going into the frequency domain. The convolution integral in Eq. (2) can also be written in the discrete summation format:

$$M_i = \sum_j R_{ij} \cdot S_j, \tag{7}$$

where R_{ij} represents the impact of the overall response function. S_j and M_i are the original signal at jth time bin and the measured signal at ith time bin. We can also write the above equation in the matrix format.

$$M = R \cdot S, \tag{8}$$

and we can simply derive the solution of S as

$$S = R^{-1} \cdot M, \tag{9}$$

where the subscript -1 represents the inversion of matrix R. We should note that the above formula is more general than that of the Fourier transformation, which requires the response matrix R to be symmetric around the diagonal line.

2.3.2. χ^2 Minimization

Solving Eq. (7) may also be written as a minimization of a χ^2 function:

$$\chi^2 = \sum_i \left(M_i - \sum_j R_{ij} \cdot S_j \right)^2. \tag{10}$$

The minimum of χ^2 can be derived as:

$$\frac{\partial \chi^2}{\partial S_k} = 0 \rightarrow \sum_i 2 \cdot \left(M_i - \sum_j R_{ij} \cdot S_j \right) R_{ik} = 0, \tag{11}$$

for any k. A solution for Eq. (7) will also solve this equation. We note this is general to the case that a filter function is included.

2.3.3. χ^2 Minimization with a Penalty Term

As we discussed previously, without a filter function the result of the deconvolution will not be numerically stable. In the χ^2 formalism a filter function can be introduced in terms of a *penalty term* in the χ^2 definition which constrains the smoothness of the solution:

$$\chi^2 = \sum_i \left(M_i - \sum_j R_{ij} \cdot S_j \right)^2 + \chi^2_{penalty}. \tag{12}$$

The penalty term can usually be expressed in the following format:

$$\chi^2_{penalty} = c^2 \left(\sum_j F_{ij} \cdot S_j \right)^2. \tag{13}$$

A generic matrix F is used to express the summation. A commonly used example of the penalty term would be the square of the second derivative of the solution:

$$\chi^2_{penalty} = c^2 \sum_i \left(S_i^{''} \right)^2. \tag{14}$$

In the discrete space, we can write this as

$$S_i^{''} \sim S_{i+1} - 2S_i + S_{i-1} \equiv \sum_j F_{ij} \cdot S_j. \tag{15}$$

Plugging Eq. 13 to Eq. (12) to derive the minimum, we have

$$\frac{\partial \chi^2}{\partial S_k} = 0 \rightarrow \sum_i \left(M_i - \sum_j \left(R_{ij} + \frac{F_{ij} \cdot F_{ik}}{R_{ik}} \right) \cdot S_j \right) \cdot R_{ik} = 0, \tag{16}$$

for any k. Similarly, the solution is

$$\sum_i \left(M_i \cdot R_{ik} - \sum_j R_{ij} \cdot R_{ik} \cdot \left(1 + \frac{F_{ij} \cdot F_{ik}}{R_{ij} \cdot R_{ik}} \right) \cdot S_j \right) = 0. \tag{17}$$

In matrix notation this is

$$R \cdot M = \left(R^2 + F^2 \right) \cdot S, \tag{18}$$

or

$$S = \left(1 + \frac{F^2}{R^2} \right)^{-1} \cdot R^{-1} \cdot M. \tag{19}$$

In comparison with Eq. (9), the above solution has an addition term of $\left(1 + \frac{F^2}{R^2}\right)^{-1}$, which depends on the penalty term in the χ^2 definition. The nature of the penalty term is to make sure the solution is smooth and stable. Such penalty terms are also called regularization terms in some literature.

2.3.4. Role of the Deconvolution Filter

Now, given the above preparation, we can evaluate the role of the deconvolution filter. First, as described in Sec. 2.2, the filter is applied to remove or suppress the contributions from certain frequencies where the noise dominates. This directly justifies its name "filter". Second, the augmentation of the response function by the filter function can be equivalently and instead written to be considered part of the signal

$$S_{filter}(\omega) = S_{nofilter}(\omega) \cdot F(\omega) \tag{20}$$

based on Eq. (6). The above equation can be converted back into the time domain:

$$S_{filter}(t_0) = \int_{\{t\}} F(t - t_0).\, S_{nofilter}(t)\, dt, \tag{21}$$

in which the estimator for the filtered signal ($S_{filter}(t)$) receives contribution from non-filtered signal ($S_{nofilter}(t)$) at various times. Written in this way, we can see that the filter function is effectively a smearing function. The application of a smearing function leads to cancellations of nearby large positive and negative values in the non-filtered signal resulting in a smoother filtered signal. Third, it can be easily seen that Eq. (19) is basically the discrete form of Eq. (21). In this case, the filter function is related to the penalty term added to χ^2 function which is to constrain the smoothness of the final solution.

Given the above understanding of the role of deconvolution filter, we can construct various filters. In particular, we constructed two filters which achieve different goals. The first filter is a *Wiener-inspired*[12] filter which is applied to maximize the signal-to-noise ratio in the deconvoluted signal in each wire plane. While conserving the signal strength in terms of integration of signal height, this filter causes some undesired negative tails in the signal. Furthermore, the Wiener-inspired filter can be different for each wire plane. The second is a *Gaussian* filter (equivalent to a Gaussian smearing function in the time domain), which doesn't cause negative tails. This choice also conserves charge and preserves the time information in the real signal. If chosen to be the same for all wire planes, one can compare the reconstructed ionization charge between different wire planes at given digitization time slice.

2.4. 2D Deconvolution for Induction Planes

The 1D deconvolution procedure described in Sec. 2.2 works well in dealing with signals in the collection plane, but is not optimal when applied to signals in the induction wire planes. As described in Sec. 1, the induction plane wire signal receives contributions not only from ionization charge passing by the wire of interest, but also from ionization charge drifting in nearby wire regions. In addition, within the wire region of interest the value of the field response function varies appreciably and so at small scales the location of the drifting charge relative to the wire is important. Ignoring the later effect, Eq. (2) can be naturally expand to

$$M_i(t_0) = \int_{-\infty}^{\infty} (R_0 \cdot (t - t_0) \cdot S_i(t) + R_1 \cdot (t - t_0) \cdot S_{i+1}(t) + ...) \cdot dt, \tag{22}$$

where M_i represents the measured signal from wire i. S_i and S_{i+1} represents the real signal inside the boundaries of wire i and its next neighbor respectively. The R_0 represents the average response function for an ionization charge passing through the wire region of interest. Similarly, the R_1 represents the average response function for an ionization charge drifting past in the next adjacent wire region. One can easily expand this definition to n number of neighbors by introducing terms up to R_n.

If we then apply a Fourier transform on both sides of Eq. (22), we have:

$$M_i(\omega) = R_0(\omega) \cdot S_i(\omega) + R_1(\omega) \cdot S_{i+1}(\omega) + ..., \tag{23}$$

which can be written in a matrix notation as:

$$\begin{pmatrix} M_1(\omega) \\ M_2(\omega) \\ \vdots \\ M_{n-1}(\omega) \\ M_n(\omega) \end{pmatrix} = \begin{pmatrix} R_0(\omega) & R_1(\omega) & \dots & R_{n-2}(\omega) & R_{n-1}(\omega) \\ R_1(\omega) & R_0(\omega) & \dots & R_{n-3}(\omega) & R_{n-2}(\omega) \\ \vdots & \vdots & \ddots & \vdots & \vdots \\ R_{n-2}(\omega) & R_{n-3}(\omega) & \dots & R_0(\omega) & R_1(\omega) \\ R_{n-1}(\omega) & R_{n-2}(\omega) & \dots & R_1(\omega) & R_0(\omega) \end{pmatrix} \cdot \begin{pmatrix} S_1(\omega) \\ S_2(\omega) \\ \vdots \\ S_{n-1}(\omega) \\ S_n(\omega) \end{pmatrix} \tag{24}$$

Now, if we assume that we know all response functions (i.e. the matrix R), the problem converts into deducing the vector of S with the measured signal M. This can be achieved by inverting the matrix R. In practice and away from plane edges the matrix R is taken to be symmetric and its inversion can again be achieved by the discrete-space techniques described in Sec. 2.3. As this expands the 1D deconvolution (with respect to the time axis) into a 2D deconvolution (with respect to both the time and wire axes) similarly we must also expand the filter function to cover both time and wire dimensions.

A comment on the limitation (or approximation) assumed in the 2D deconvolution is needed. As shown in Eq. (22), the average response functions are used in describing the measured signal. These ignore the

detailed position dependence of the response function. This approximation ignores the fine grained but clear position dependence in the calculated weighting fields. However, since we can only measured the signal from any given wire as a function of time there is no additional information to be used to resolve the ionization electron distributions within a wire region at this stage. This technique can in principle be improved to include the position dependent response once the local ionization charge distribution is roughly reconstructed. Currently, we did not explore this possibility.

2.5. Additional Challenges in Deconvolution

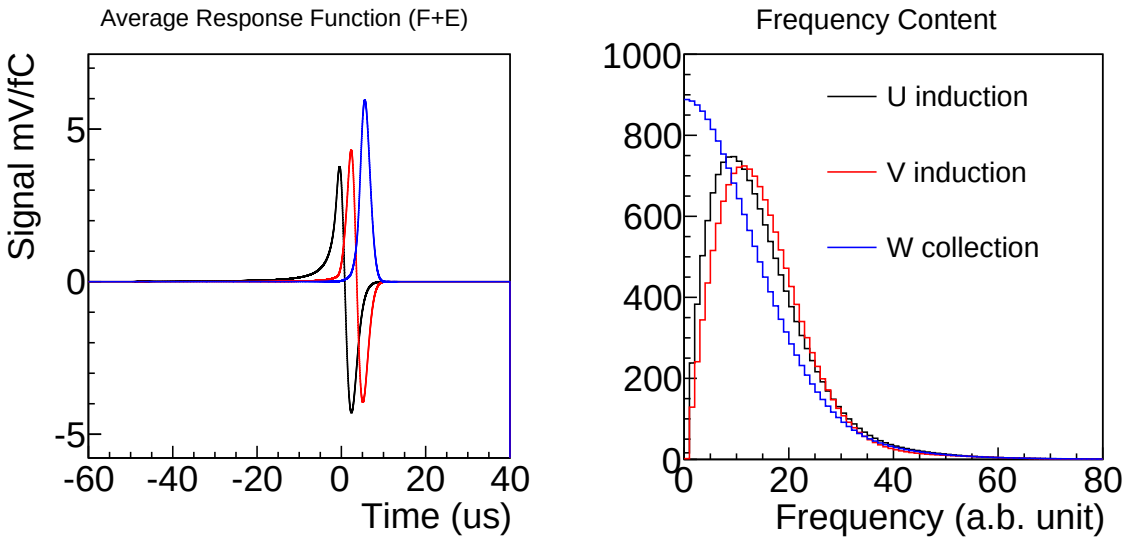

FIG. 4. (left) Examples of simulated field response functions for induction (black and red) and collection (blue) wires are shown in the time domain. (right) The same are shown in the frequency domain.

The 1D and 2D deconvolution procedures provide a robust method to extract the ionization electrons for the collection and induction planes, respectively. While working well for the collection plane the procedure is still not optimal for the induction plane due to the nature of the induction plane signal. Figure 4 shows the field response as simulated by Garfield for induction and collection wire planes and point ionization electrons without diffusions. While the field response for the collection wire plane is uni-polar, the field response for the induction wire plane is bipolar. The early, positive half corresponds to the ionization electron moving towards the wire plane and the late, negative half corresponds to the ionization electron moving away. The integration of the field response function is close to zero as the bias wire voltages are applied such that that none of the ionization electrons are collected. The right panel of Fig. 4 shows the frequency components of the field response. Since an induction plane field response has a bipolar shape in the time domain there is a corresponding suppression at low frequency in the frequency domain. At zero frequency, the frequency component essentially gives the integration of field response function over time and thus should be near zero (again, because no charge is collected).

The suppression of the induction field response at low frequency is problematic for the proposed deconvolution procedure. First, as shown in Ref. [10], the measured signal contains the electronic noise, which usually increases at low frequency (the so-called 1/f noise). Therefore, as shown in Eq. (6), the low frequency noise will be amplified in the deconvolution process, since the denominator (i.e. the induction field response) is generally small at low frequency. This can be seen clearly in Fig. 5, where the low frequency noise is significant. The large low frequency noise would lead to large uncertainty in the charge estimation and needs to be dealt with. We considered three ways to deal with this problem.

2.5.1. Using An Imbalanced Response Function

As described above, it is the balanced and bipolar nature of the induction response which leads to it being small at low frequencies and it is this which then can enhance the noise. It's natural to then imagine using an intentionally imbalanced field response in the deconvolution procedure. As it turns out, this is indeed

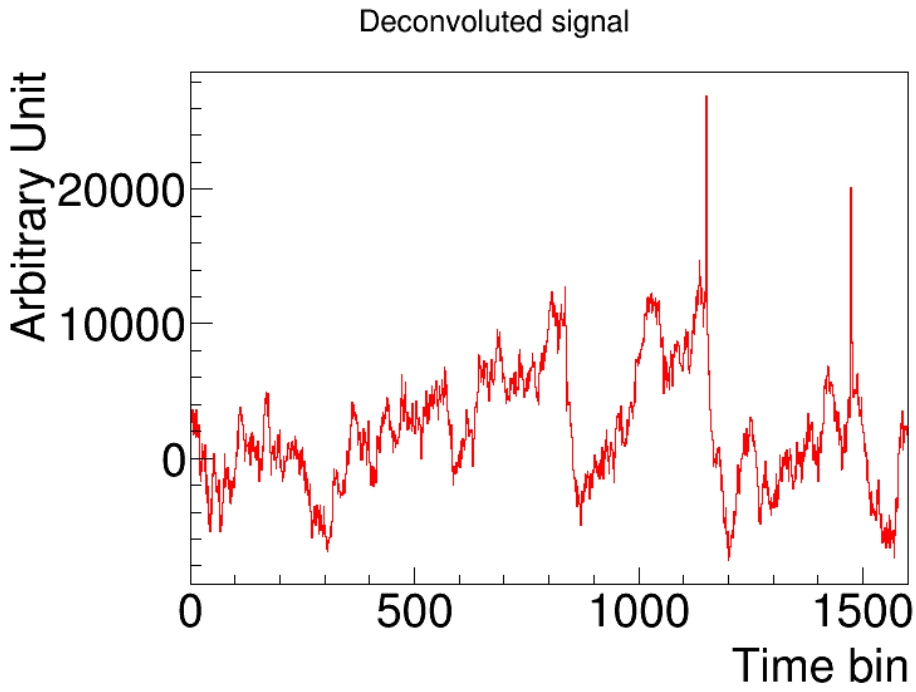

FIG. 5. An example deconvoluted spectrum for the induction plane.

what has been done initially with 1D average field response. Figure 6 shows the deconvoluted signal on the induction plane with an imbalanced field response function. As expected, the low-frequency noise is effectively suppressed. However, the mismatch of the field response function used in the deconvolution and the actual physical field response leads to a distortion of the signal. In this figure, a stopping muon is shown. The blue shadow below the muon track is due to the distortion. Near the vertex where the muon stops and is captured, there is a clear gap and which is indicated on the figure. The appearance of the gap is due to the negative tail of the large muon capture signal totally canceling the signal arising from the nearby end of the muon track. Therefore, this approach is not sufficient as it introduces large distortions in the deconvoluted image. On the other hand, one may consider investigating hardware solution of intentionally allowing some portion of drifting ionization charge to be collected on the induction wires. The detailed discussion of this possibility is beyond the scope of this technote and is omitted.

2.5.2. Low-frequency Software Filter

In Eq. (6), a frequency-domain filter function is introduced to suppress the numerical instability caused by the presence of noise. One can imagine to use this software filter to suppress the electronic noise at low frequency. This is also not optimal due to large distortion introduced on the signal. To understand this point, we recall the discussion in Sec. 2.3; the software filter is effectively a smearing function. Figure 7 shows an illustrative real signal (left), its convolution with a low-frequency filter (middle), and the low-frequency filter itself (right). It is obvious that the signal is strongly distorted due to the application of the low-frequency software filter (such as the strictly defined Wiener filter).

2.5.3. Region Of Interests (ROI) and Adaptive Baseline (AB)

In the previous two sections, we show that we cannot suppress the low-frequency electronic noises with either the intentionally imbalanced response functions nor the low-frequency software filter. Instead we turn to two techniques in the time domain: region of interest and adaptive baseline.

The region of interest (ROI) technique was proposed by Bruce Baller in the context of reducing data size and speeding up the deconvolution process. At the same time, the ROI technique can also be used to suppress the low frequency noise. In order to recognize this point, we consider a time window with N time

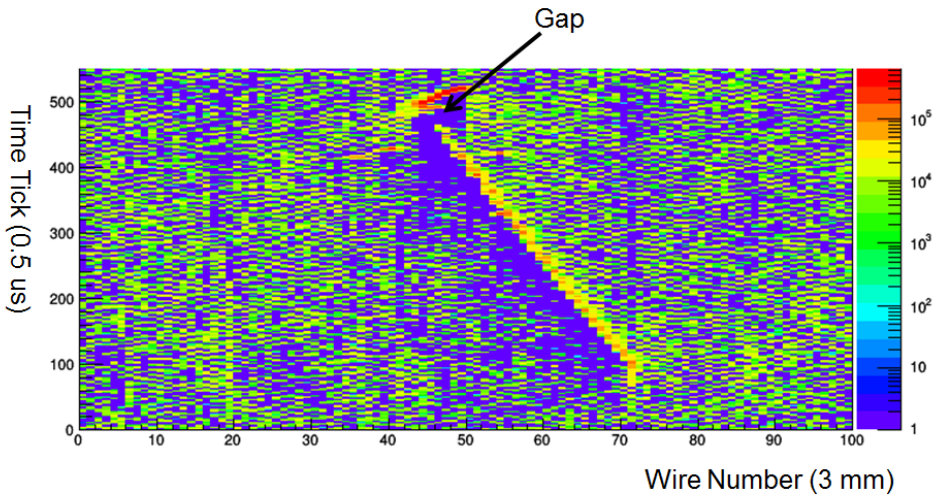

FIG. 6. Deconvoluted induction plane signal using an imbalanced field response function. X and Y axis represents the wire and drift time, respectively. See text for more discussion.

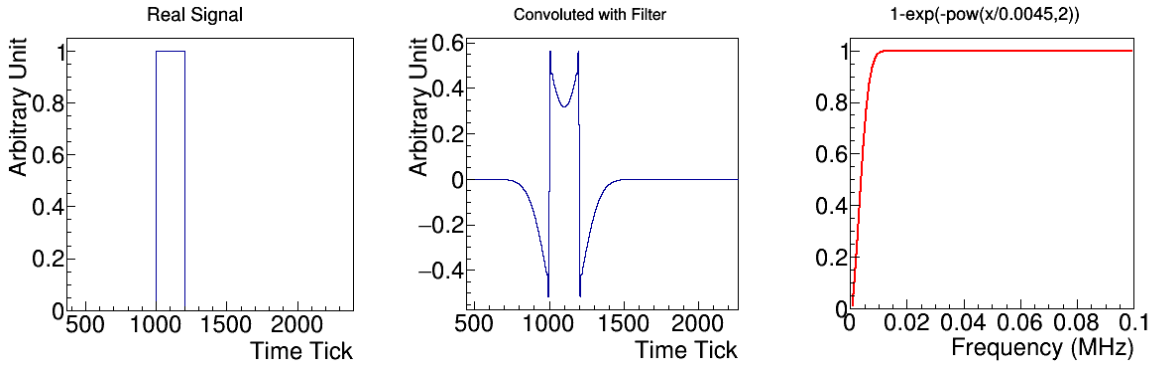

FIG. 7. The impact of the low-frequency filter (right). The unit of the X-axis is MHz. The real signal and the convoluted signal are shown in the left and middle panel, respectively. A time tick is 0.5 μs.

ticks. For MicroBooNE this would be a window of $N \times 0.5\mu$s. The highest frequency that can be resolved with such sampling would be 1 MHz. The first discrete frequency above zero is be $2/N$ MHz and no result within the ROI can be sensitive to any noise components below this frequency. Therefore, if we can identify the signal region and create a ROI to cover the signal, we can naturally suppress the low-frequency noises.

The adaptive baseline (AB) technique was introduced by Mike Mooney in the context of dealing with the ASIC saturation [10]. The AB is essentially a local baseline calculated in a given a ROI. However, instead of a simple average of the baseline at the start and end points of a ROI, a linear interpolation is used to correct the baseline. Given the two constraints (start and end points of the ROI), the linear interpolation with two degrees of freedom is the best that one can achieve to remove bias in the baseline.

In the following section, we discuss the implementation of the these techniques.

2.6. Algorithm Implementation in Wire-Cell

The Wire-Cell [13] is a new reconstruction package being developed to perform 3D tomographic reconstruction for LArTPC events. Currently, there are four major reconstruction steps: i) TPC Signal Processing including both the noise filtering and drifted-charge extraction, which is common for any reconstruction method, ii) Tomographic 3D Image Reconstruction, iii) 3D pattern recognition, and iv) Calculation of physics quantities given the identified pattern. Detailed description of the Wire-Cell reconstruction will be reported in another technote in the future.

Figure 8 shows the overall flow of the drifted-charge extraction algorithm. Details of the noise filtering can be found in Ref. [14]. Here, each time tick corresponds to 0.5 μs. Each merged ticks contain six time ticks, thus 3 μs. This choice is governed by the overall drift HV and the electronics shaping time, which is 2 μs. The default choice for Wire-Cell is 4 time ticks at 500 V/cm electric field. However, MicroBooNE is currently running at 273 V/cm, so it is enlarged to 6 time ticks, as the field response spans over larger time. Note, during the deconvolution process, we essentially replace the field response functions with the filter functions. The information lost through the smearing process cannot be recovered with the deconvolution. To select the ROIs, we use both 1D deconvolution with data-driven 1D field response function and the 2D deconvolution with Garfield simulated response function with a low-frequency filter. Once the ROIs are selected, the results of the 2D deconvolution without the low-frequency filter are updated with the adaptive baseline technique. The description of the electronics response function and field responses (both 1D and 2D) can be found in Sec. 2.6.1 and Sec. 2.6.2, respectively. To select "Hit" (the signal at a particular time slice measured in merged ticks is required to above certain threshold) and calculate its corresponding charge, different software filters are used. They are described in Sec. 2.6.3. The details regarding the ROI selection is elaborated in Sec. 2.6.4. The procedure to extract hit and its corresponding charge is described in Sec. 2.6.5. In Sec. 2.6.7, we describe the calibration of the relative time offset (using "Hit") and relative normalization (using "Charge" given "Hit") for field response functions among wire planes. In Sec. 2.6.6, we show the performances on the data.

2.6.1. Calibration of Electronics Response Function

The electronic response function has been discussed in detail in Ref. [10].

The electronics response function for the MicroBooNE detector is shown in Fig. 9 in terms of signal amplitude vs. time at a given gain. The MicroBooNE front-end cold electronics are designed to be programmable with four different gain settings (4.7, 7.8, 14, and 25 mV/fC) and four shaping-time settings (0.5, 1, 2, and 3 us). The shaping time is defined as the time between peak and 5% of the peak in the falling edge. For a fixed gain setting, the peak is always at the same height independent of the shaping time.

2.6.2. Calculation of Field Response Function

There are two sets of field responses used in the actual implementation. The first set is data-inspired response function. The second set is the Garfield-simulated response functions. The importance of using 2D field response function has been introduced in Sec. 1. In the drift direction, the two induction planes wire planes are labeled U and V and the collection plane is Y. The data-inspired response functions are shown in the left panel of Fig. 10. In this case, the shape of the overall response function, which includes both electronics and field responses, is adjusted according to a few randomly picked pulses from the data. They were used as the traditional 1D response function. For U and V planes, these response functions are quite unbalanced. As discussed in previous sections, they cannot satisfy the needs for the drifted-charge extraction in induction wire planes. In the second case, the field response is calculated by Garfield [9] in a 22 cm (along the field direction) $\times$ 30 cm (along the wire plane direction) region in 2D. The spacing between the planes is 3 mm. The bias voltages of -110 V, 0 V, and +230 V for the U, V, and Y planes, respectively, are configured according the operating conditions which ensure 100 % transmission of ionization electrons through the first two induction planes. 101 wires with 150 μm diameter are set on each wire plane with 3 mm pitch. The drift field is uniform with 273 V/cm. The electron drift velocity as a function of electric field is taken from measurements [15, 16] instead of using the default velocity table contained in Garfield. The electron diffusion is turned off in the simulation. The field response function then can be calculated for each individual wire in the form of induction current (U and V planes) and collection current on (Y planes) as a function of time for an electron drift which starts from arbitrary position within the region of calculation. The average response function for single electrons within a wire region (over 12 different locations) is then calculated for the closest wire R_0, next adjacent wire R_1, and so on. The U and V plane responses functions are shown in the middle and right panel of Fig. 10, respectively. For induction wire planes, these response functions are reasonably balanced as expected.

In the actual implementation, both 1D and 2D response functions are used. Ideally, there is no need to use the 1D data-inspired response function. However, there exists coherent electronics noise in MicroBooNE data [10]. It can be suppressed by performing a coherent noise removal across groups of 48 channels [10]. This procedure has a pathology where it will suppress the actual signal for a track traveling parallel to the wire plane. Special algorithms, as discussed in Ref. [10], are implemented to protect the signal. Despite these efforts, there is still a residual distortion of the signal. For example, on the U induction plane the

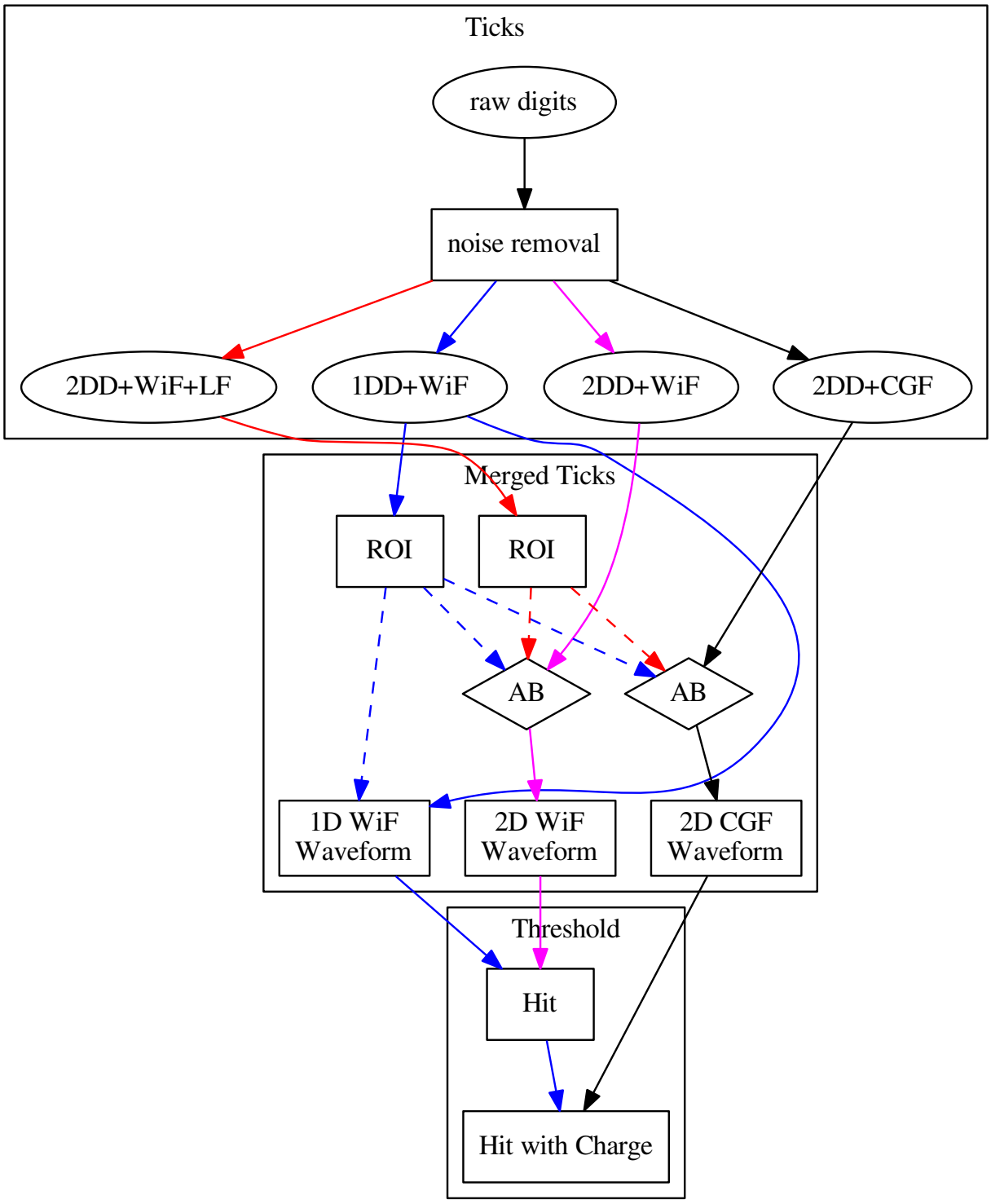

FIG. 8. Diagram illustrating the basic flow of the drifted-charge extraction for induction wire plane. Here "CGF" stands for the common Gaussian filter. "WiF" stands for the Wiener inspired filter. "LF" stands for low frequency filter. See Sec. 2.6.4 for more information.

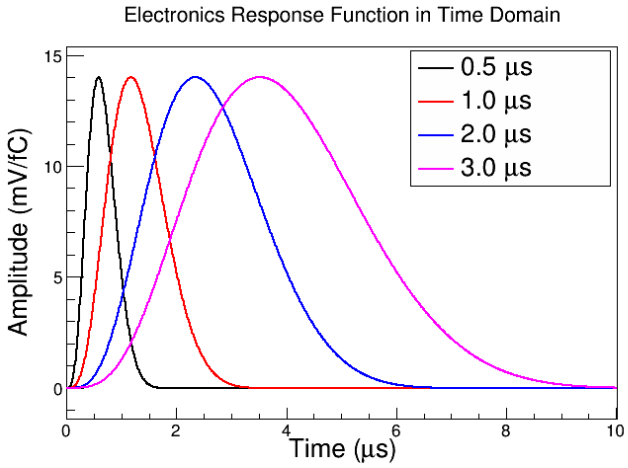

FIG. 9. ASIC's electronics shaping functions are shown for four shaping time settings at 14 mV/fC gain.

positive half of the signal is in general much smaller than the negative half of the signal. It is thus much more difficult to differentiate the positive half of the signal from the electronics noise. Apparently, the distortion is the largest for the tracks traveling parallel to the wire plane. With these distortions, the 2D deconvolution sometimes has trouble resolving small signals from parallel tracks. In this case, we go back to the traditional 1D deconvolution with 1D data-inspired response function to mitigate this defect.

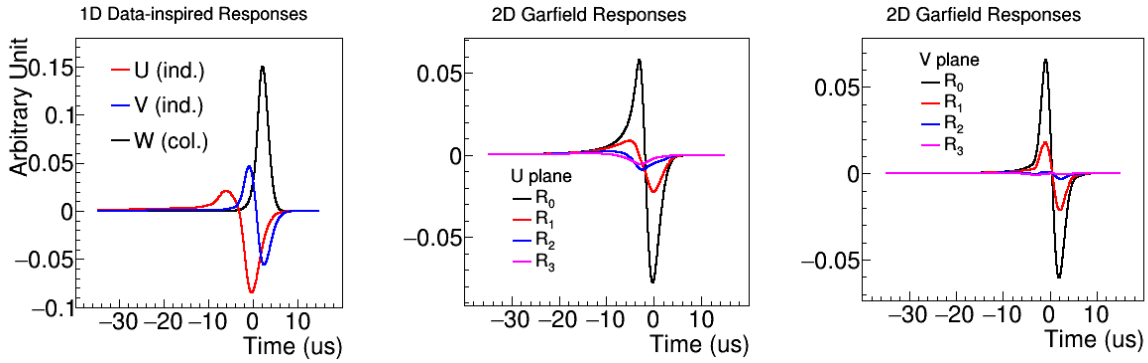

FIG. 10. The overall response functions, which is the convolution of the electronics response function (14 mV/fC gain and 2 μs shaping time) and the field response, are shown. See text for more discussion.

2.6.3. Choice of Software Filter

As discussed above, we select and implement two types of filters. The first is inspired by the Wiener filter. It is modified to not suppress low frequency components. The second one is the Gaussian filter. While the first one is optimized for each wire plane to produce a high signal-to-noise ratio, the second one is optimized and is the same for all the planes to correctly estimate the charge which is independently measured on each of the three planes. This latter point is important if all three planes are used for energy measurement, as is required for proper application of the Wire-Cell imaging technique. In this section, we describe the choice on these software filters.

The standard Wiener noise filter [12] is constructed using the expected signal $S(\omega)$ and noise $N(\omega)$ frequency spectra:

$$F(\omega) = \frac{S^2(\omega)}{S^2(\omega) + N^2(\omega)}. \tag{25}$$

With this construction, the Wiener filter is expected to achieve the best signal to noise ratio. However, naively applying the Wiener filter to TPC signal processing is problematic. Firstly, in LArTPC, the TPC

signal $S(\omega)$ varies substantially depending on the exact nature of the event topology. Secondly, the electronic noise spectrum is a function of the time window over which it is observed. A longer time window allows for observation of more low frequency noise components. Thirdly, the induction wire signal spectrum is small at low frequency and so would be its Wiener filter. As discussed in Sec. 2.5.2, a software filter with low-frequency suppression leads to large distortions of the signal and is thus not ideal.

The functional form of the software filter is chosen as:

$$F(\omega) = \begin{cases} e^{-\frac{1}{2}\cdot\left(\frac{\omega}{a}\right)^b} & \omega > 0 \\ 0 & \omega = 0, \end{cases} \tag{26}$$

with a and b are two free parameters. Note, $b = 2$ is basically the Gaussian filter. The filter is explicitly zero at $\omega = 0$ in order to remove the DC component in the deconvoluted signal. This removes information about the baseline and a new baseline is calculated and restored for the waveform after deconvolution. The above functional form of the filter has another advantageous property:

$$lim_{\omega\to 0} F(\omega) = 1. \tag{27}$$

which means the integral of the smearing function is unity, which does not introduce any extra factor in the overall normalization. The free parameter a and b in the above form is determined by fitting the tail of Wiener filter at its high frequency side. For U plane, we have a = 14.36 and b = 4.95. For V plane, we have a = 14.74 and b = 4.98. For Y plane, we have a = 14.59 and b = 5.02. The time window is chosen to be 200 time ticks (or 100 μs). The signal is assumed to be a minimal ionized track ($\sim$ 2.1 MeV/cm [17]) traveling parallel to the wire plane and over a distance of one wire pitch (3 mm). The noise model is from Ref. [10] for the longest wire ($\sim$ 5 m length).

The final software filter is shown in Fig. 11 and Fig. 12.

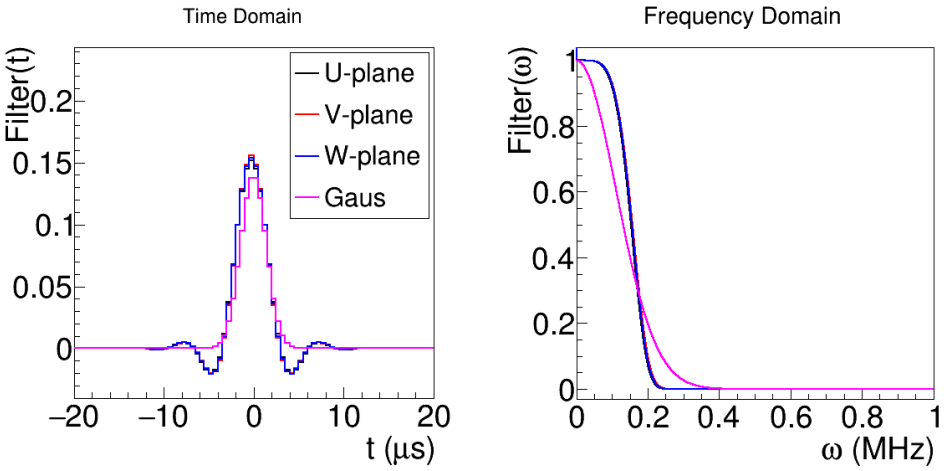

FIG. 11. The Wiener-inspired filter and Gaussian filter used in the 1D deconvolution. The time and frequency domain content are shown on the left and right panel, respectively. The x-axis's unit for the time domain is μs. For the frequency domain, the number 2000 corresponds to $\sim$0.42 MHz.

Beside the high-frequency software filter described above, there is also a low-frequency software filter which is only used to select ROIs (discussed in the next section). The functional form of the low-frequency software filter is

$$F(\omega) = 1 - e^{-\frac{1}{2}\cdot\left(\frac{\omega}{c}\right)^2}, \tag{28}$$

with c = 4.5 kHz. The distortion of such a low-frequency software filter has been shown in Fig. 7.

2.6.4. ROI Selection

As discussed in Sec. 2.5.3, the region of interest (ROI) is an important technique to limit the contribution of low-frequency electronic noise to treat induction signal. The traditional ROI selection is based on the

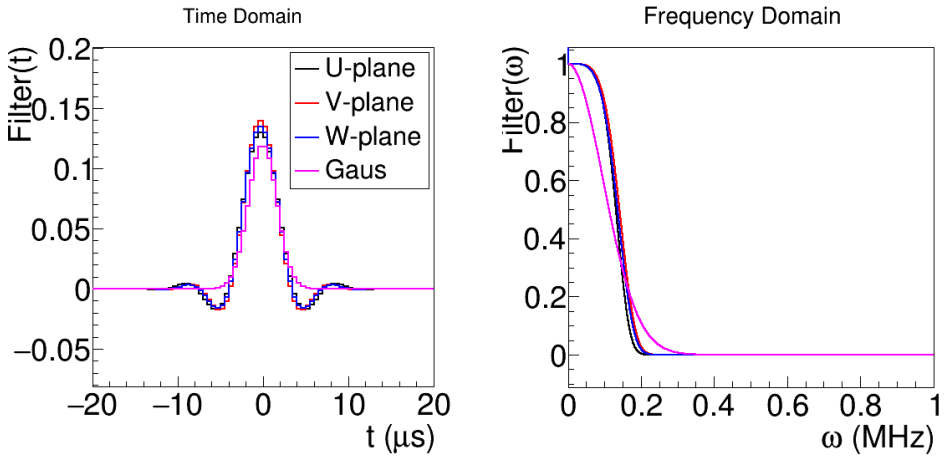

FIG. 12. The Wiener-inspired filter and Gaussian filter used in the 2D deconvolution. The time and frequency domain content are shown on the left and right panel, respectively. The x-axis's unit for the time domain is μs. For the frequency domain, the number 2000 corresponds to ∼0.42 MHz.

raw-digit waveform. In this case, the seed of each ROI is selected by locating bins in the raw digits which are above certain threshold values. However, this choice does not apply well to induction plane signals as explained in the following.

Figure 13 shows an example of an ideal track (in the direction of the red arrow) with a uniform charge distribution along the track. On the left panel, the two black lines represent the boundaries of one wire region. If one just counts the ionization charge distribution within the wire region, the expected signal is illustrated in the panel a) on the right. However, as we discussed in Sec. 1, the induced current on the wire of interest depends on the weighting field, which is smaller when the ionization electron is further away from the wire itself. Therefore, the effective charge distribution seen by the wire would be similar to the panel b). The story does not end here. Now, for ionization electrons drifting by in the near-by wires regions, the wire of interest will also experience a further induced current. In this case, since the ionization electrons are further away from the target wire, the weighting field is even smaller and thus their induction is also smaller. The realistic effective charge distribution will be similar to the panel c) on the right.

We can then see what happens to the raw digits when we take into account the bipolar induction field response function. In the left panel of Fig. 14, the top half illustrates the real charge distribution going through the targeted wire region. The convolution of this distribution with a bipolar response function will lead to results illustrated at the bottom. We can see the signal height is still large at least for the start and the end of the signal. However, in the right panel of Fig. 14, the top half illustrates a more realistic effective charge distribution seen by the targeted wire. The convolution of this distribution with a bipolar response function will lead to results shown at the bottom. We can see that the signal height is much smaller although the length of signal is long. A threshold-based ROI selection will likely to miss such signal which leads to gaps in the reconstructed images of the event activity in the LAr volume.

In order to avoid the aforementioned ROI selection inefficiency, the ROI selection is based on deconvoluted signals with Wiener-inspired filter (WiF). We perform three rounds of deconvolution:

- 1D deconvolution with the imbalanced data-driven field response function ("1DD").
- 2D deconvolution with the balanced Garfield-simulated field response function with a low-frequency filter ("2DD+LF").
- 2D deconvolution with the balanced Garfield-simulated field response function without a low-frequency filter ("2DD").

The ROI selection is based on applying a threshold on the result of "1DD" and "2DD+LF". In "1DD", the low frequency noise is suppressed due to using the imbalanced field response. In the "2DD+LF", the low-frequency noise is suppressed with the low-frequency software filter. The upper left, middle, and right panel of The ROI selection is performed with the following procedure:

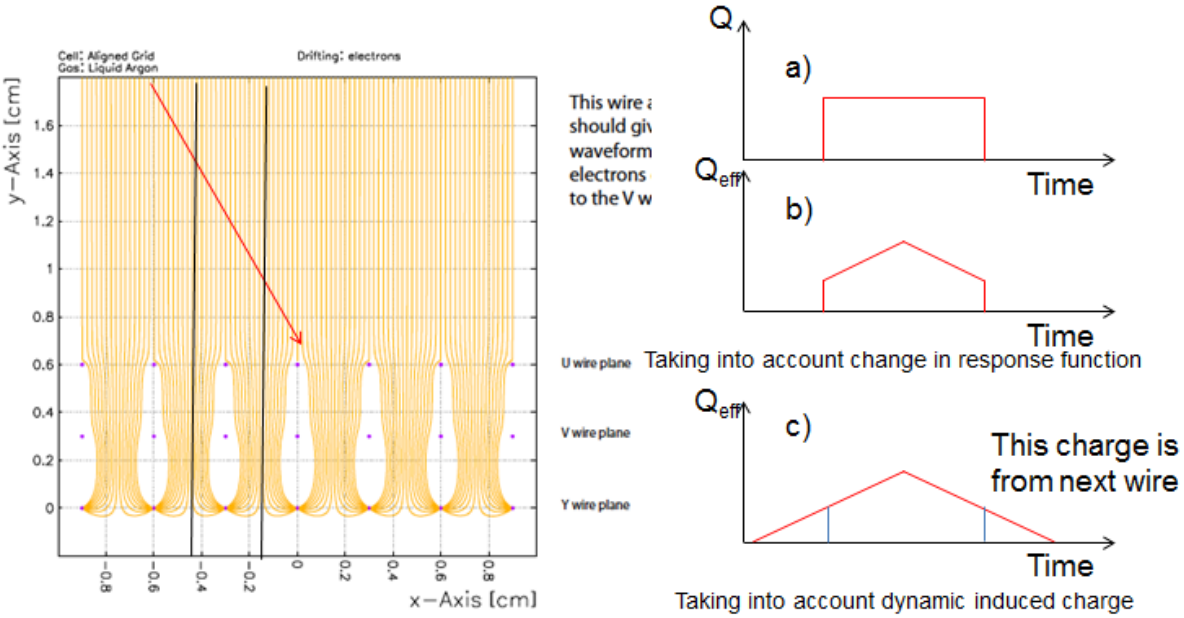

FIG. 13. Illustration of the induction plane field response for an ideal track. See text for more discussion.

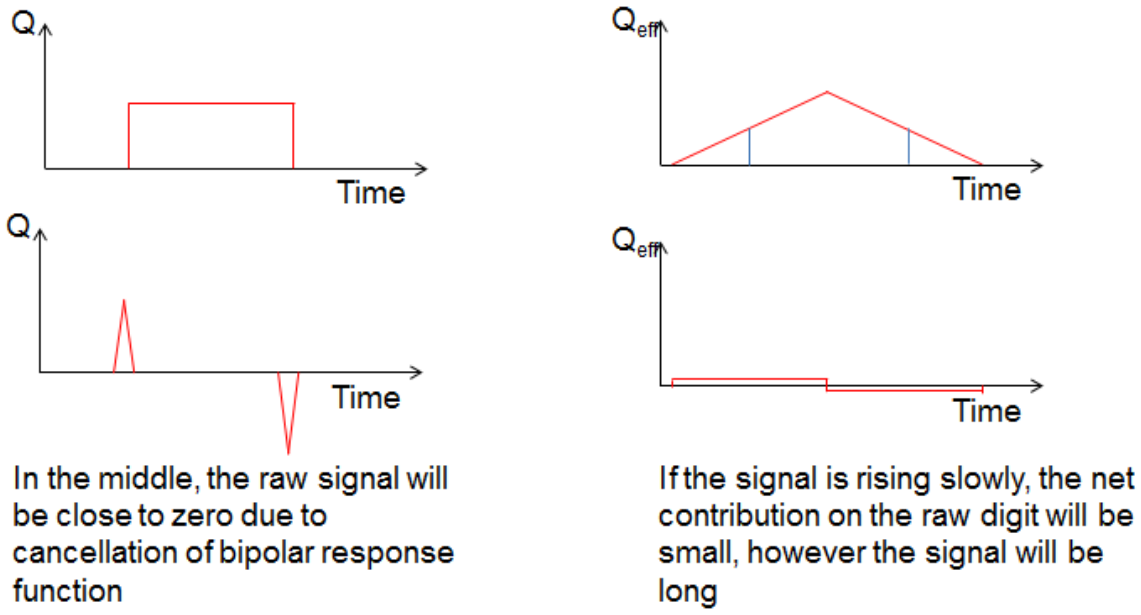

FIG. 14. Illustration of the induction plane field response for an ideal track. See text for more discussion.

- The seed of ROI is chosen by applying a threshold on each of the histogram. For "1DD", the threshold is based on 3.6 times of the corresponding RMS noise. For "2DD+LF", the threshold is based on 2.0 times of the corresponding RMS noise. The choices of threshold are made through looking at the performance of ROI selection on a few events and can in principle be further optimized.
- The ROI region is then expanded from the seed to both side. A local average is calculated for every 3 near-by time bins (each time bin is corresponding to six time ticks). The ROI expansion will stop if the local average is the local minimum (smaller than the nearby averages).
- Given the determined ROIs from "2DD+LF" or "1DD", the content from the "2DD" was filled after applying the adaptive baseline technique. A peak finding using the "TSpectrum" package [18] was

further applied to the resulting histogram. Smaller ROIs are formed if there multiple visible peaks found within the ROI, and the adaptive baseline is further applied to the smaller ROIs. The final histogram content inside the ROI was further examined according to the 4.0 times of the corresponding RMS noise of "2DD+LF" histogram. Note the threshold was chosen at 2.0 times of the RMS for the "2DD+LF". Since there are two sets of ROIS (one from "1DD" and one from "2DD+LF"), two histograms are generated, one for each set of ROIs. They are i) "2DD" + "1DD" ROI and ii) "2DD" + "2DD+LF" ROI. These two histograms are merged into "2D WiF Waveform" as shown in Fig. 8 by choosing the largest content at each time slice.

- Given the determined ROIs from "1DD", the above procedure was repeated using the content from "1DD". The "1D WiF Waveform" as shown in Fig. 8 is generated.

- In the final step, the two histogram ("2D WiF Waveform" and "1D WiF Waveform") are further merged together by choosing the largest content among these two histograms at each time slice. We should note that the content of the histograms outside the ROI is essentially zero.

We should note that there are many "magic" numbers used in the ROI selection. These magic number are currently obtained by a combination of educated guesses from the estimated signal to noise ratio and experiences gained in looking at many 2D images after deconvolution and 3D images after Wire-Cell imaging. These magic numbers can in principle be optimized with a realistic noise and induction signal simulation, which is not available at this moment. Once this simulation is available, the reconstructed 2D images can be compared with MC truth in order to evaluate the efficiency and purity as a function of these "magic" numbers.

2.6.5. Hit and Charge Extraction

Once the ROIs are selected, we can extract hits and their associated charge. Two rounds of 2D deconvolution with the balanced Garfield-simulated field response function without a low-frequency filter were performed. The only difference between these two rounds are the software filter. In the first round, which aims at the hit finding, Wiener-inspired filters, which are optimized individually for each wire plane, are used. In the second round, which aims at the charge extraction, a common Gaussian filter, which is chosen to be the same for all three wire planes, is used. The other components including: i) the field response function, ii) the electronics response function, iii) ROIs, are the same between these two rounds of 2D deconvolution to ensure the hit and charge information are matched.

The result of the first round of 2D deconvolution was used to choose hits. A hit is defined when a wire waveform at a particular time slice is above a pre-chosen threshold. A time slice is measured in merged time ticks (six in current MicroBooNE running condition). For the current implementation, we use the 3.6 times the of the corresponding RMS noise of "1DD" as the threshold. Once a hit was found, the corresponding charge information was obtained from the result of the second round of 2D deconvolution at the exact same time bin.

As shown in Fig. 8, two sets of ROIs (one from "1DD" and the other from "2DD+LF") are used to extract the charge information. Basically, two histograms are generated with the same procedure as described in previous section with each set of ROIs. The two histograms are then merged according to the largest content at each time slice.

2.6.6. Performance on MicroBooNE Data

In this section, we show the performance of the aforementioned drifted-charge extraction procedure on the MicroBooNE data by showing examples from two events. Figure 15 shows a likely neutrino interaction in MicroBooNE (run 3493, sub-run 821, event 41075) viewed by the first induction plane (U). The left panel shows the raw digits after the noise removal as described in Ref. [10]. The middle panel shows the deconvoluted results based on 1D deconvolution and imbalanced data-driven field response function. In this event, there is a track traveling at a large angle with respect to the wire plane (i.e. large coverage in the drift time and small coverage in the wire number). It is clear that a portion of this track is below the noise level in the raw digits. The segment is not recovered by the traditional deconvolution procedure. The right panel shows the results from the new procedure described in this technote. In this case, the large-angle track is clearly visible. In addition, the overall image is much sharper than the first two panels. Similarly, Fig. 16 shows a stopping muon viewed by the second induction plane (V). In the traditional deconvoluted result (middle panel), there is a gap below the muon capture region, which is due to using the incorrect

(imbalanced) field response function. The image is much sharper for the new procedure (right panel). Based on these results, it is clear that the new drifted-charge extraction procedure significantly improves the image quality, which will lead to a much better performance in the latter event reconstruction chain.

As an example of an interesting anomaly, in Fig. 16, we can see a vertical tail at bottom of the muon track. This part is corresponding to the case when the muon track is going through the anode wire plane. From the raw digits, we can only see the negative signals (blue) in the first time bin, which only includes the parts the ionized electrons leaving the induction plane. This part was misinterpreted to be a long tail given the standard bipolar field response function used in the deconvolution.

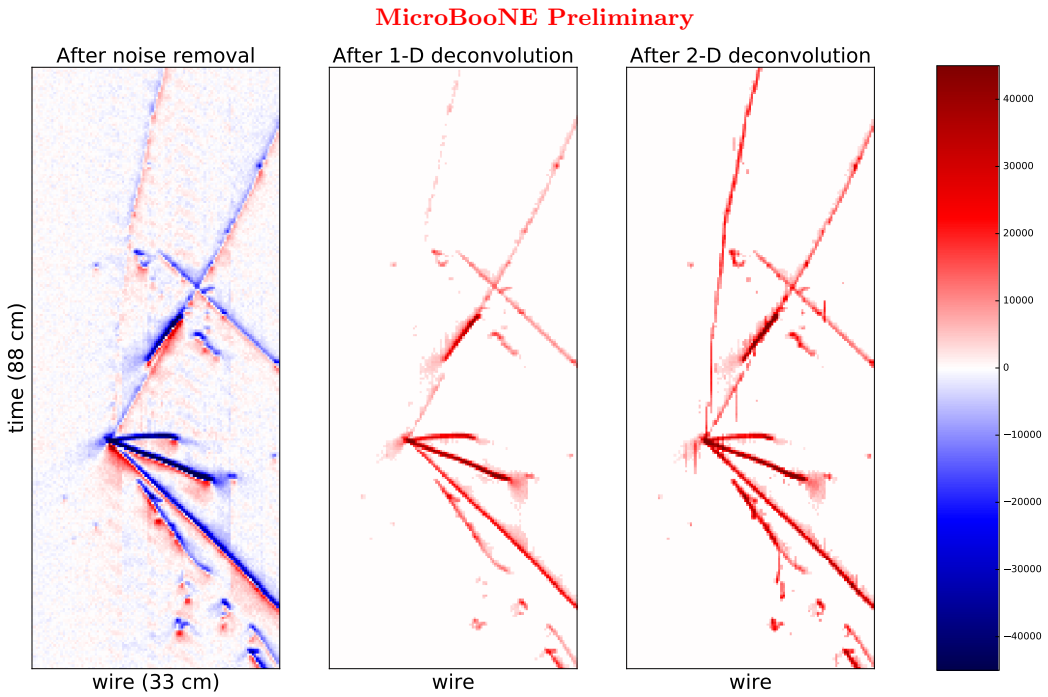

FIG. 15. Run 3493, sub-run 821, event 41075. The y-axis is the time in ticks. The x-axis is the wire number. This is the U induction plane image. See Sec. 2.6.6 for more discussion.

2.6.7. Relative Calibration Among Multiple Planes

In the TPC drifted-charge extraction procedure, the response functions are required to be known. The shape of the data-driven response function for "1DD" is based on the comparison with real data. The shape of the Garfield-simulated response function for "2DD" is obtained by averaging point response functions simulated by Garfield. Although the shape of the response functions is known, the relative time offsets among the induction U, induction V, and collection Y are not known (at least for the data-driven response function). In addition, the relative normalization of the field response function is also not known. In this section, we

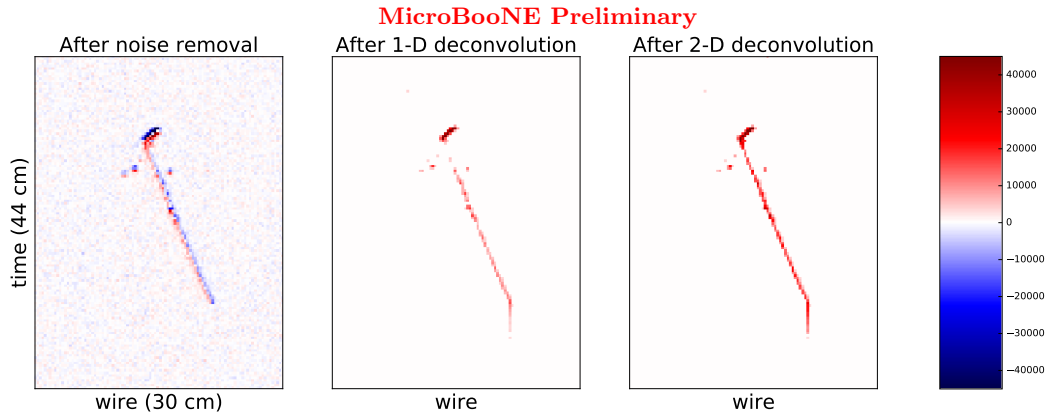

FIG. 16. Run 3455, sub-run 0, event 6. The y-axis is the time in ticks. The x-axis is the wire number. This is the V induction plane image. See Sec. 2.6.6 for more discussion.

describe the procedure that we used to calibrate these time offsets and the relative normalization among wire planes.

The Wire-Cell reconstruction provides a natural framework to perform such inter-plane calibrations. The crucial observation is that the same element of charge drifts past the two induction planes and is collected on the collection plane, and furthermore the signal times in the three planes have essentially fixed offsets. The Wire-Cell technique allows the signals in the three planes to be associated, with a common charge for each. This is done by dividing up perpendicular projection of the three planes into "cells" centered on the intersection of the wires, and then merging the cells to deal with diffusion and non-perpendicular drift paths between the planes. The inter-plane timing can be adjusted to maximize the number of hit cells. For example, a time shift in the field response function would lead to a time shift in the location of the corresponding hit and thus lead to a mist-match hits among three planes, which will reduce the number of cells reconstructed.

The discrepancy of simulated time offset among the Garfield-simulated field responses and the calibrated time offset is observed and indicates that there are differences between the simulated response function and the data. This also draws attentions on how reliable is the shape of the simulated response function. As discussed in Sec. 1, the induction current is described by the Shockley-Ramo theorem, in which the product of the weighting field vector and the velocity vector of the ionization electrons is involved. The discrepancy between the simulated and calibrated time offset essentially indicates that the model of the drifting velocity (to be more precise, the simulation of the external drifting field) doesn't describe the data. Therefore, one expects that the simulated shapes of induction currents also deviate from reality. It is therefore crucial to develop a program to calibrate the TPC field response directly for the current and future generation of LArTPCs.

We further calibrate the relative normalization of the field response by comparing the the measured charge vs. the predicted charge on the wire. This is possible because the predicted charge is calculated assuming all three wire planes are seeing the same amount of ionization charge.

3. METRICS IN EVALUATING TPC SIGNAL PROCESSING

In order to evaluate the TPC signal processing, which include both the noise filtering and the drifted-charge extraction, there are two robust metrics that can be used to evaluate TPC signal processing (which includes both the noise filtering and the drifted-charge extraction):

- Equivalent Noise Charge (ENC):
  ENC is basically proportional to the pedestal RMS in terms of ADC, and is a direct measure of the

noise level in the unit of electrons. It can be used to compare the noise levels from different experiments.

- Deconvoluted Noise Charge after the TPC drifted-charge extraction (DNC):
  The goal of the TPC drifted-charge extraction process is to recover the number of ionization electrons from the measured TPC signal. With the same procedure, the electronic noise will also be converted. The unit of these noise is again electrons, which can be compared with the expected ionization electrons from energetic charge particles. As described in this technote, the DNC depends on the ENC as well as the frequency content of the noise spectrum. It also depends on the response function used for deconvolution. This is the primary reason why the induction plane DNC is much higher than the collection plane DNC. Furthermore, since we have to rely on ROI and AB techniques to reduce the noise level for the induction plane, DNC also depends on the time window length of ROI.

Understanding the ENC and DNC for the current-generation experiments and the expected performance for the future experiments are important steps to achieve automated event reconstruction for LArTPCs.

The ENC in MicroBooNE has been reported at Ref. [10]. As illustrate above, the calculation of DNC depends on the drifted-charge extraction procedure. More specifically, it depends on the field response, the noise level (ENC and the frequency content), and the length of ROI. Fig. 17 shows the calculated DNC as a function of the time window length for the second induction (V) plane, which is expected to have the smallest field response function (thus the largest DNC). The noise model used in this simulation is described in Ref. [10], and the ENC is conservatively chosen to be 500 electrons, which is higher than that has been achieved in MicroBooNE.

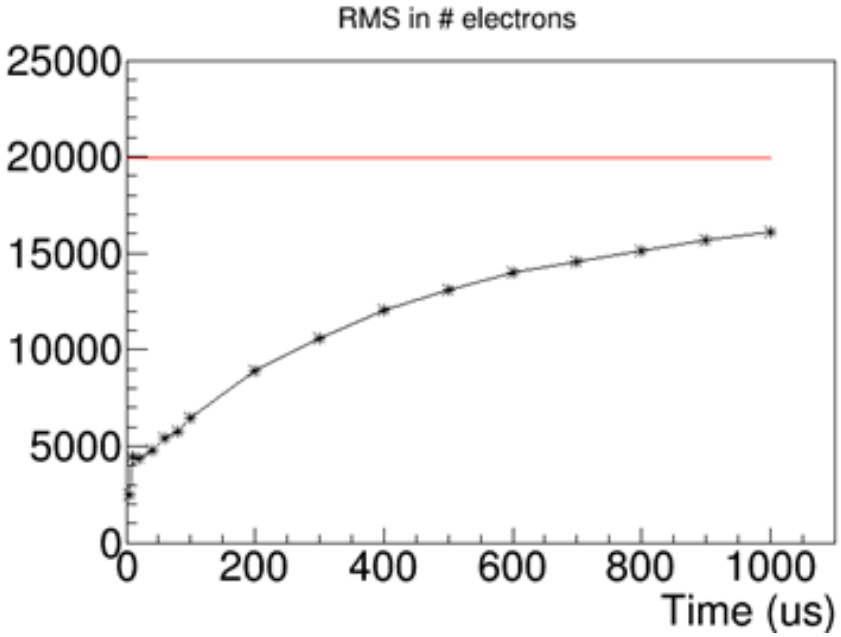

FIG. 17. Calculation of DNC with respect to the time window length for second induction (V) plane. The ENC used in this simulation is 500 electrons which is higher than the ENC achieved in MicroBooNE. The red line shows the expected signal size for a minimal ionizing particle (MIP) traveling 3.2 mm.

4. FUTURE DEVELOPMENTS

In this section, we outline some anticipated future developments:

- Calibration of the TPC field response functions:
  As shown in previous sections, some of 2D induction images after drifted-charge extraction contain shadows near regions with large drifted charge. These shadows are believed to be due to inductions since the weighting field can extend quite far beyond the corresponding wire region. Furthermore, the time offset calibration of the simulated response function also shows clear deviations. These facts all point to imprecise field response functions, which need to be improved in the future. We plan to attack

this problem from two directions. Firstly, we will work on a TPC field response calibration device with a laser-drive photo cathode in a local test stand at BNL. Secondly, we could try again to calibrate the TPC field response with cosmic muons using some advanced numerical techniques. As illustrate in this technote, we made some initial attempts to calibrate the TPC field response with cosmic muons, but encountered many difficulties including unknown absolute charge normalization, impacts from the digitization, and numerical difficulties to invert large-dimension matrix.

- The "magic" numbers used in the ROI selection and the hit selection should be optimized:
  The optimization can be achieved once the development of a more realistic simulation in terms of electronic noise as well as induction signal modeling is available. In this case, the "magic" numbers can be optimized by comparing the reconstructed charge vs. the MC truth to evaluate the efficiency and purity (i.e. fake hits). In addition, the algorithm itself can in principle be fine tuned during this process.

- Evaluation of charge resolution:
  With a more realistic simulation, we can also evaluate the charge resolution after the drifted-charge extract procedure by comparing the extracted charge vs. the MC truth.

Furthermore, the next steps in the overall Wire-Cell reconstruction chain is i) 3D imaging, ii) 3D pattern recognition, and iii) calculation of physics quantities such as angle and dE/dx. The 3D imaging use the time, geometry, and charge information to construct 3D objects directly. The procedure is less sensitive to the electronics noise and some noises introduced due to the imperfection of the drifted charge extraction procedure, as the exact match of time and geometry from three planes is required. For example, electronics noise in one of the plane is difficult to be matched with the other planes. At the same time, the procedure is more sensitive to the efficiency of the charge extraction procedure. If signal from one wire plane is missed, the corresponding 3D point is missed. We can then evaluate the 3D imaging reconstruction efficiency and purity. With the development of 3D pattern recognition (still in progress), we can start to use metrics such as tracking efficiency and purity to evaluate the performance. Lastly, with the reconstructed track and shower, we need to develop the calculation of physics quantities to evaluate the angular resolution and energy resolution. It is clear that there is a long way to go to achieve fully automated high-quality event reconstruction. We are making solid progress toward this goal.

5. SUMMARY

In this technote, we described the concept and general strategy of LArTPC drifted-charge extraction, which converts the raw digitized TPC waveform to the number of ionized electrons passing through the wire plane at a given time. The proper recovery of the number of ionized electrons from all wire planes is important to the success of the subsequent reconstruction algorithms. A number of building blocks for the processing algorithm are described and characterized.

An example of implementation of the algorithm was realized inside the Wire-Cell reconstruction package. The performance was qualitatively illustrated on MicroBooNE data with event display pictures, which shows significant improvements. Some metrics to evaluate the performance of the TPC signal extraction procedure are described. Next steps towards quantification of the effect of the proposed concept and optimization of the procedure are outlined, which will be address in a future technote.

6. APPENDIX I: EXAMPLES OF 2D EVENT DISPLAY

In this section, we present 2D event displays for a few selected events. It is clear that the images after the new deconvolution procedure is significantly improved (sharper and more comprehensive) than that after the old procedure. Nevertheless, in the induction plane, there are a few low-charge blobs (as shown in Fig. 18, Fig. 21, Fig. 22, Fig. 24) which suggests the existence of induced signals beyond the closest wire. This is deduced from the fact that the blobs always show up at the early time slice. These blobs can also be seen clearly in the raw digits. The existence of these blobs in the images after the 2D deconvolution procedure indicates that the 2D deconvolution does not totally remove the induced signals beyond the nearest wire. This is likely because the shape of the field response functions used in the 2D deconvolution procedure doesn't describe the data well, which has been indicated in Sec. 2.6.7. Gaps in the images are due to unusable channels.

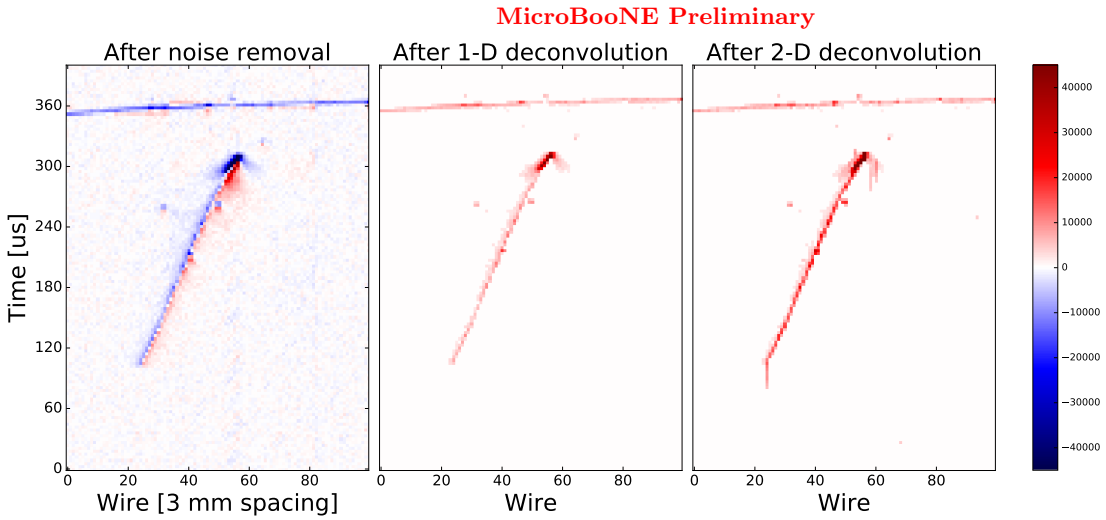

FIG. 18. 2D event display of U plane from Event 6, Run 3455. (left) 2D view from the raw digits after the noise filtering. (middle) 2D view from the deconvoluted signal with the old 1D procedure. (right) 2D view from the deconvoluted signal with the new procedure described in this technote. A blue shadow can be seen on the right side of stopping muon's capture vertex on the raw digits image on the left, this is presumably due to induction signals on nearby wires.

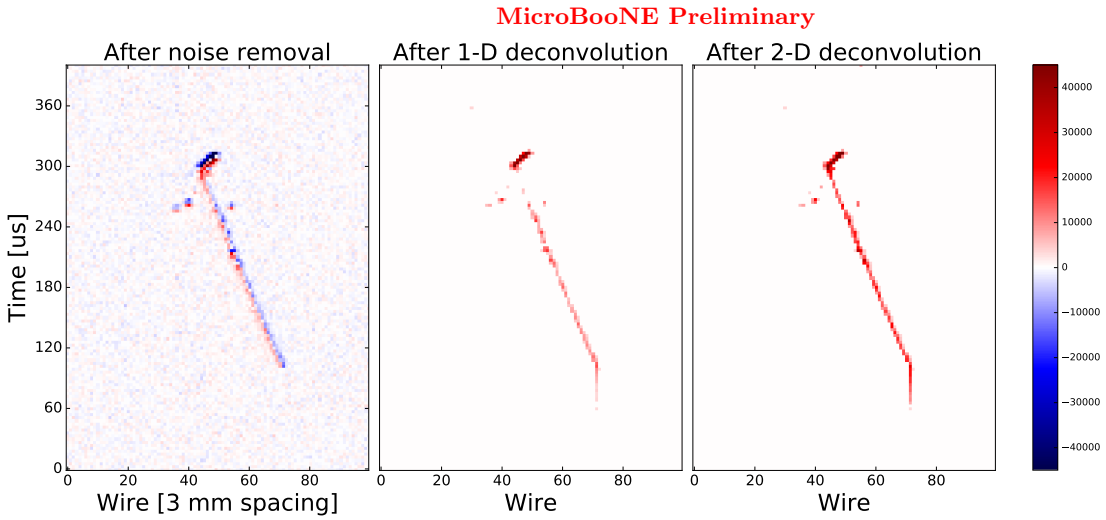

FIG. 19. 2D event display of V plane from Event 6, Run 3455. (left) 2D view from the raw digits after the noise filtering. (middle) 2D view from the deconvoluted signal with the old 1D procedure. (right) 2D view from the deconvoluted signal with the new procedure described in this technote.

7. APPENDIX II: EXAMPLES OF 2D EVENT DISPLAY FOR ELECTROMAGNETIC SHOWERS

Gaps in the images are due to unusable channels.

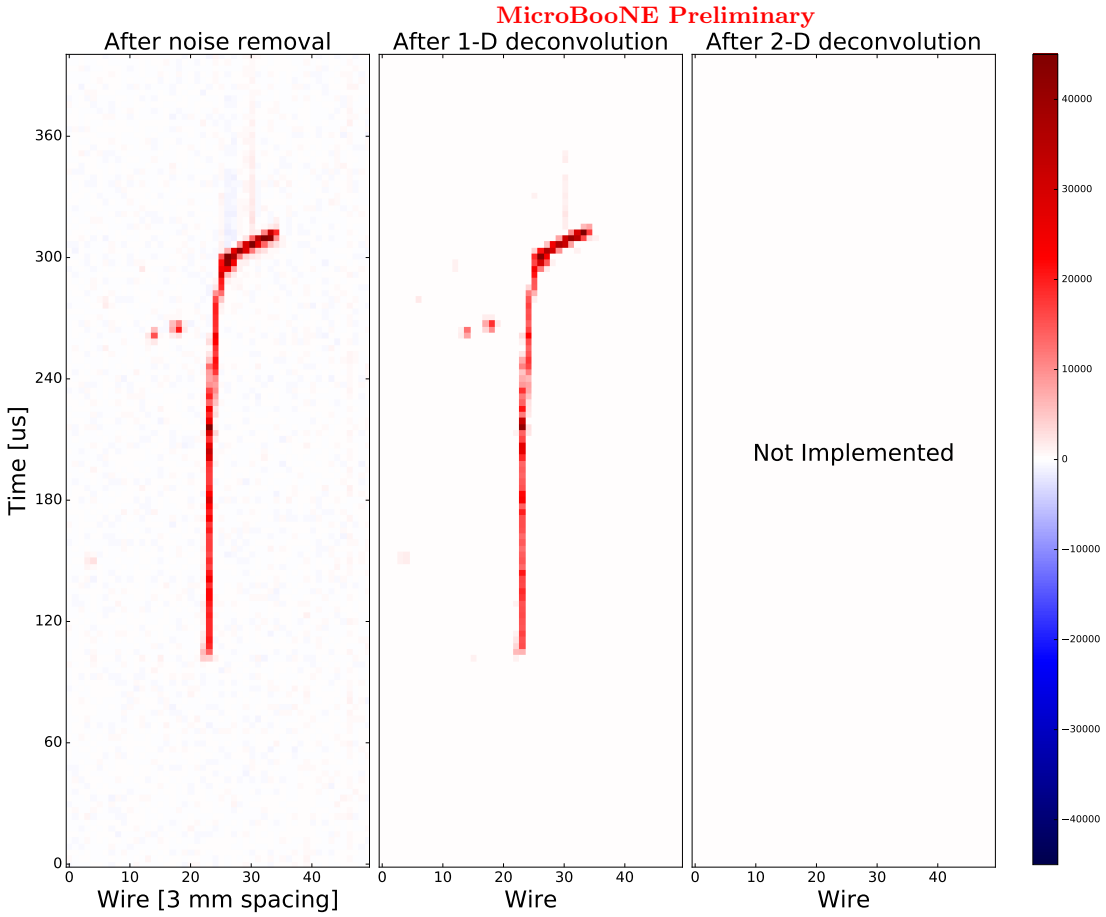

FIG. 20. 2D event display of Y plane from Event 6, Run 3455. (left) 2D view from the raw digits after the noise filtering. (middle) 2D view from the deconvoluted signal with the old 1D procedure. (right) For collection plane, the 2D deconvolution is not necessary.

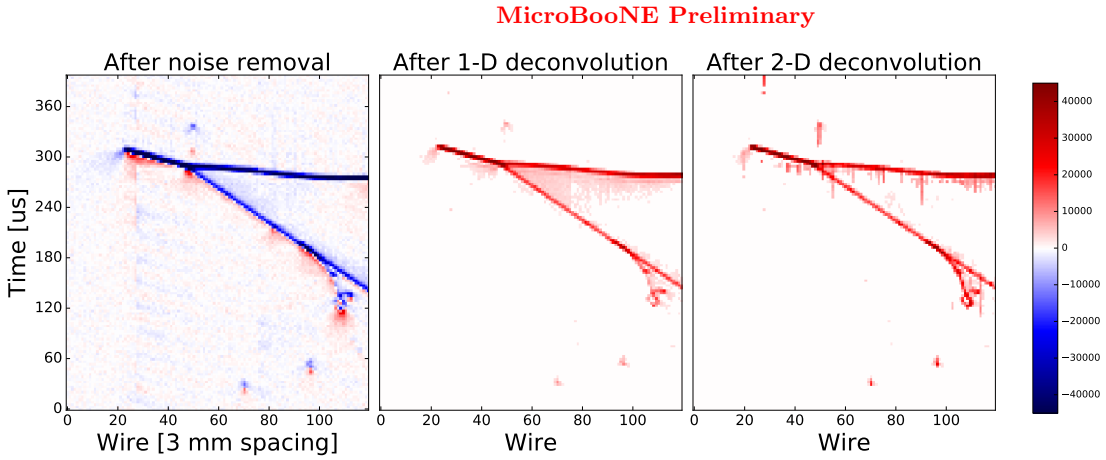

FIG. 21. 2D event display of U plane from Event 53223, Run 3469. (left) 2D view from the raw digits after the noise filtering. (middle) 2D view from the deconvoluted signal with the old 1D procedure. (right) 2D view from the deconvoluted signal with the new procedure described in this technote. A blue shadow can be seen on the end of the left-most track in the raw digit images on the left, this is presumably due to induction signals on nearby wires.

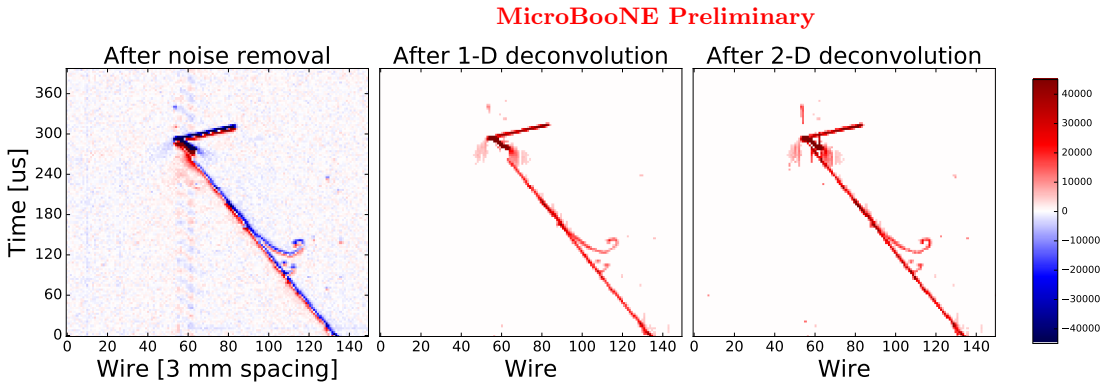

FIG. 22. 2D event display of V plane from Event 53223, Run 3469. (left) 2D view from the raw digits after the noise filtering. (middle) 2D view from the deconvoluted signal with the old 1D procedure. (right) 2D view from the deconvoluted signal with the new procedure described in this technote. Two blue shadows can be seen on raw digits, they are likely the result of induction signal on nearby wires.

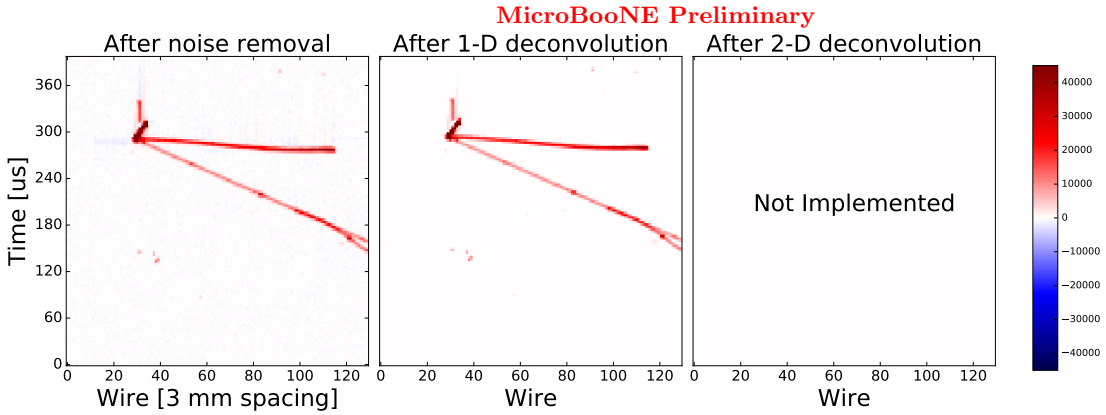

FIG. 23. 2D event display of Y plane from Event 53223, Run 3469. (left) 2D view from the raw digits after the noise filtering. (middle) 2D view from the deconvoluted signal with the old 1D procedure. (right) For collection plane, the 2D deconvolution is not necessary.

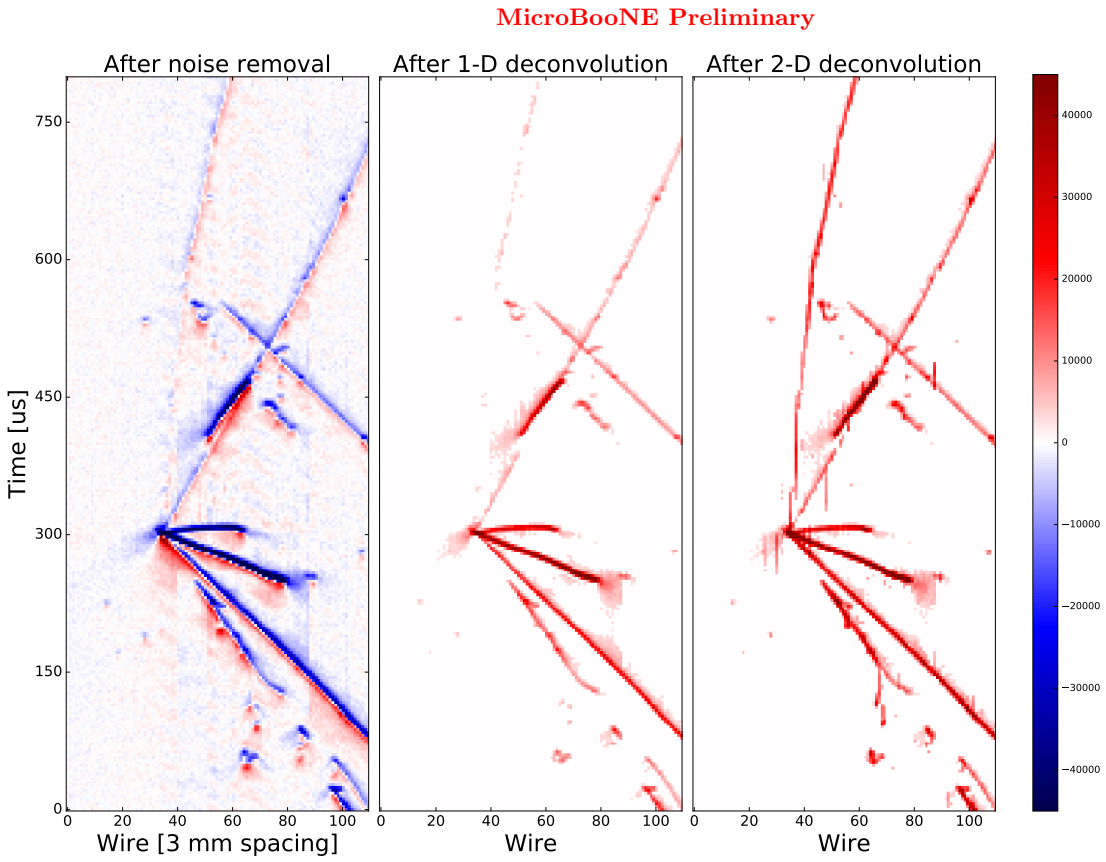

FIG. 24. 2D event display of U plane from Event 41075, Run 3493. (left) 2D view from the raw digits after the noise filtering. (middle) 2D view from the deconvoluted signal with the old 1D procedure. (right) 2D view from the deconvoluted signal with the new procedure described in this technote. Four blue shadows can be clearly seen on the raw digits image on the left. They are likely the result of induction signal on the adjacent wires.

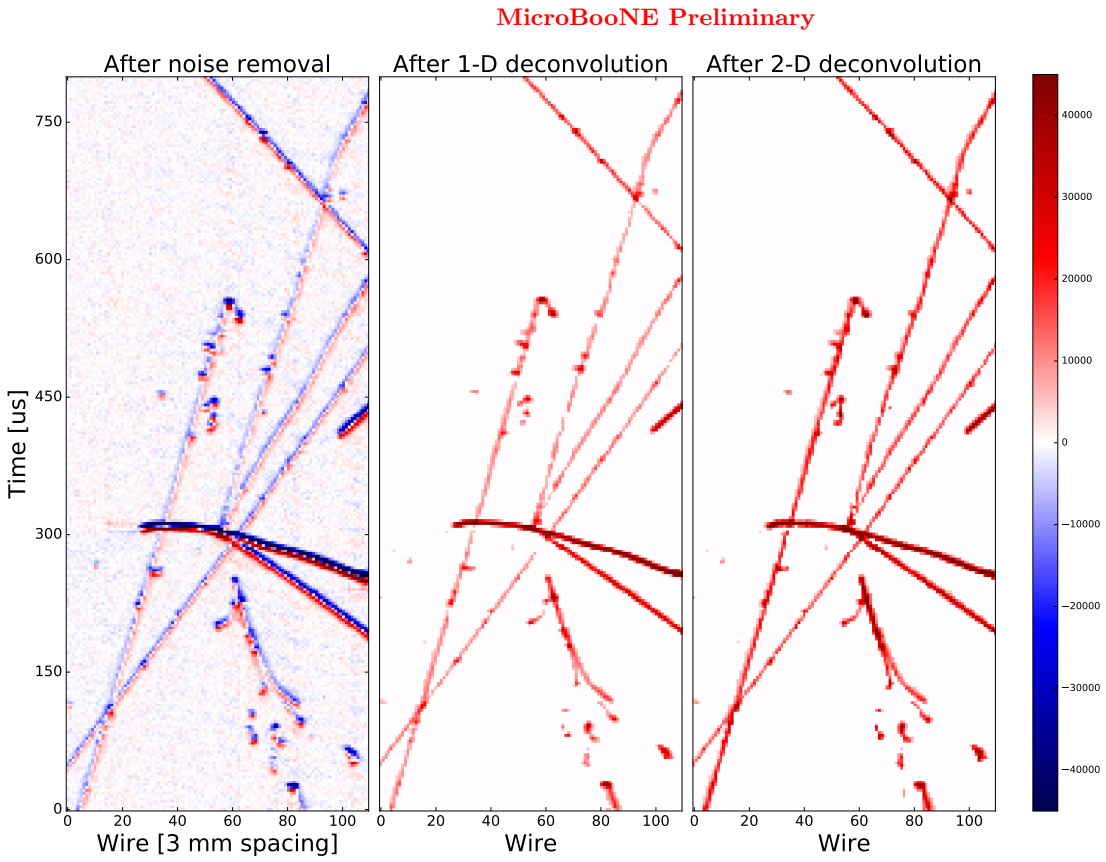

FIG. 25. 2D event display of V plane from Event 41075, Run 3493. (left) 2D view from the raw digits after the noise filtering. (middle) 2D view from the deconvoluted signal with the old 1D procedure. (right) 2D view from the deconvoluted signal with the new procedure described in this technote.

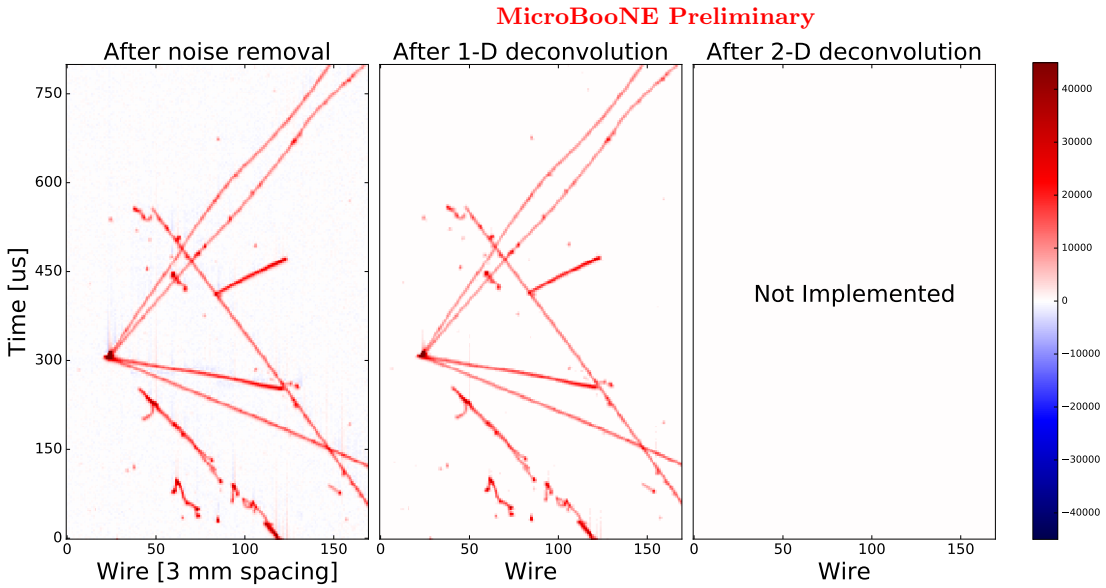

FIG. 26. 2D event display of Y plane from Event 41075, Run 3493. (left) 2D view from the raw digits after the noise filtering. (middle) 2D view from the deconvoluted signal with the old 1D procedure. (right) For collection plane, the 2D deconvolution is not necessary.

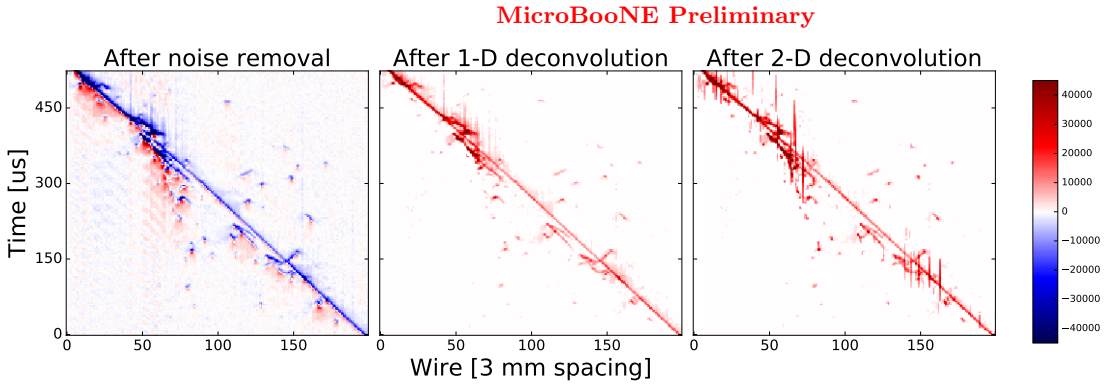

FIG. 27. 2D event display of U plane from Event 6, Run 3455. (left) 2D view from the raw digits after the noise filtering. (middle) 2D view from the deconvoluted signal with the old 1D procedure. (right) 2D view from the deconvoluted signal with the new procedure described in this technote.

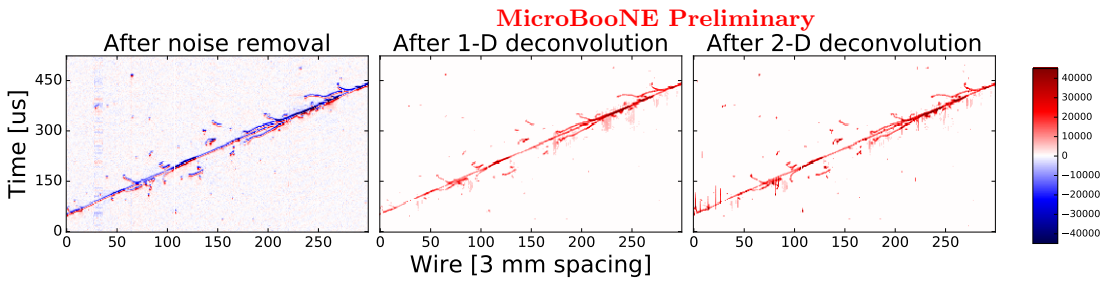

FIG. 28. 2D event display of V plane from Event 6, Run 3455. (left) 2D view from the raw digits after the noise filtering. (middle) 2D view from the deconvoluted signal with the old 1D procedure. (right) 2D view from the deconvoluted signal with the new procedure described in this technote.

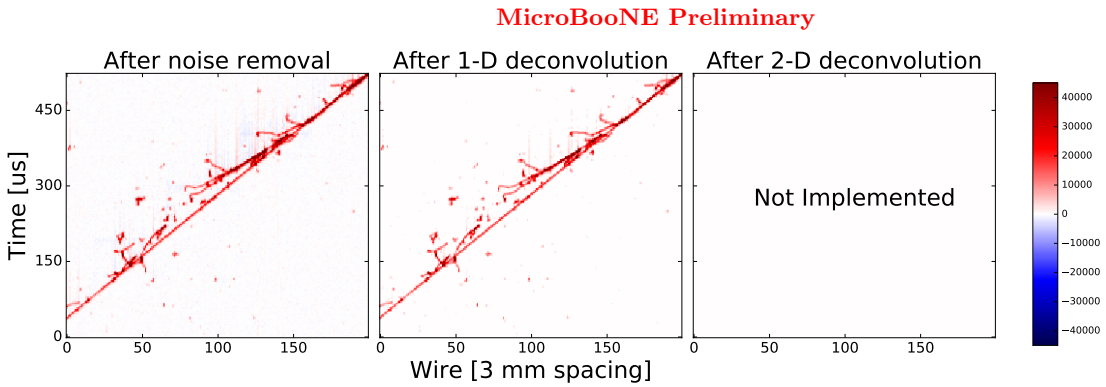

FIG. 29. 2D event display of Y plane from Event 6, Run 3455. (left) 2D view from the raw digits after the noise filtering. (middle) 2D view from the deconvoluted signal with the old 1D procedure. (right) For collection plane, the 2D deconvolution is not necessary.

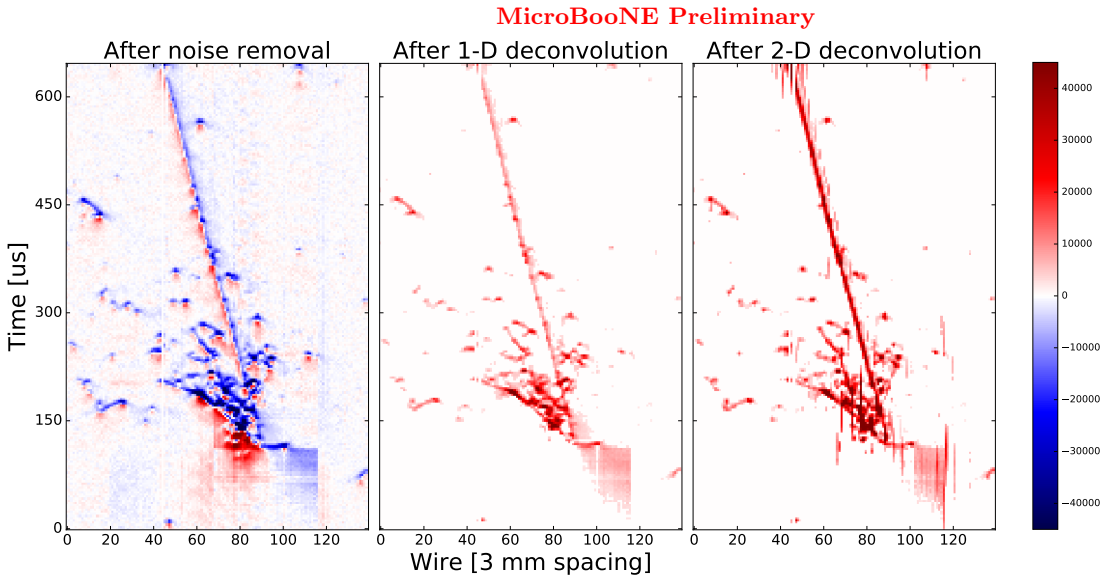

FIG. 30. 2D event display of U plane from Event 41075, Run 3493. (left) 2D view from the raw digits after the noise filtering. (middle) 2D view from the deconvoluted signal with the old 1D procedure. (right) 2D view from the deconvoluted signal with the new procedure described in this technote.

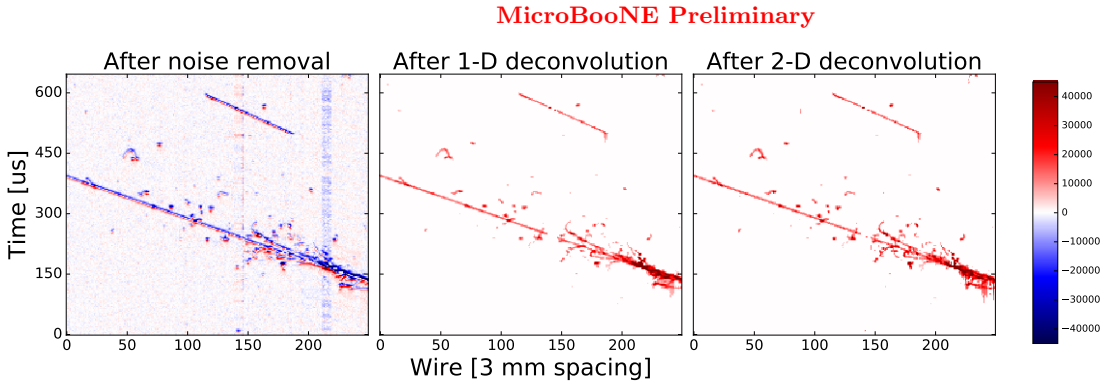

FIG. 31. 2D event display of V plane from Event 41075, Run 3493. (left) 2D view from the raw digits after the noise filtering. (middle) 2D view from the deconvoluted signal with the old 1D procedure. (right) 2D view from the deconvoluted signal with the new procedure described in this technote.

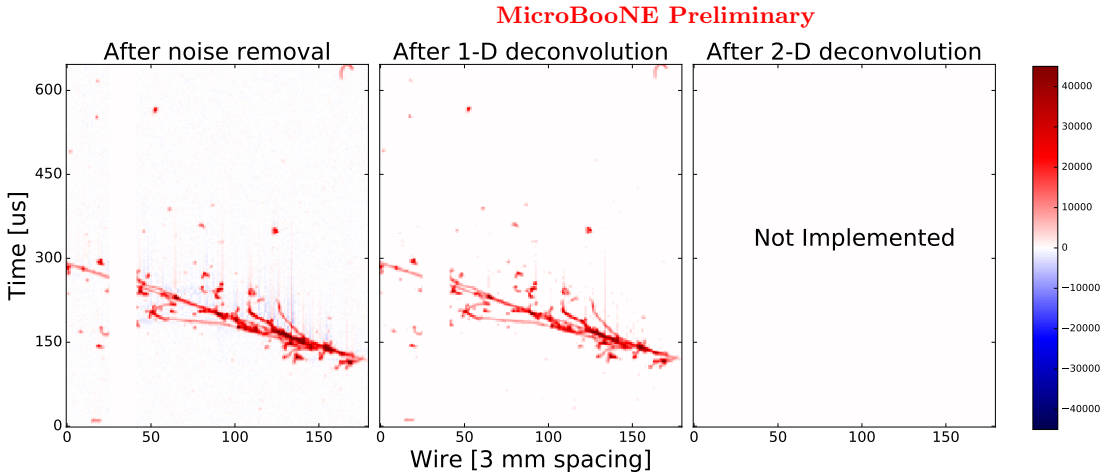

FIG. 32. 2D event display of Y plane from Event 41075, Run 3493. (left) 2D view from the raw digits after the noise filtering. (middle) 2D view from the deconvoluted signal with the old 1D procedure. (right) For collection plane, the 2D deconvolution is not necessary.

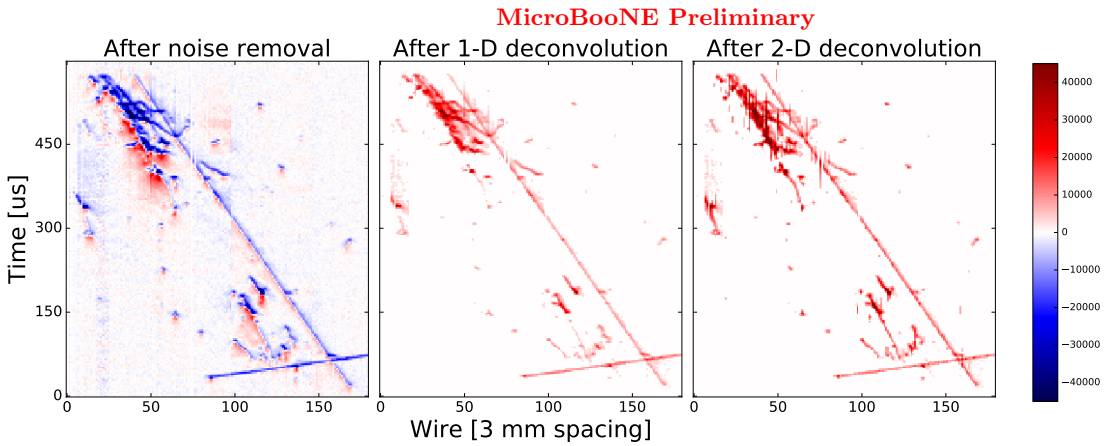

FIG. 33. 2D event display of U plane from Event 41075, Run 3493. (left) 2D view from the raw digits after the noise filtering. (middle) 2D view from the deconvoluted signal with the old 1D procedure. (right) 2D view from the deconvoluted signal with the new procedure described in this technote.

8. APPENDIX III: EXAMPLES OF 2D EVENT DISPLAY FOR π^o

In this section, we display some of the π^o events selected by the golden π^o analysis [19]. Gaps in the images are due to unusable channels.

[1] W. J. Willis and V. Radeka. Liquid argon ionization chambers as total absorption detector. *Nucl. Instrum. Meth.*, 120:221, 1974.
[2] D. R. Nygren. The Time Projection Chamber: A New 4 pi Detector for Charged Particles. *eConf*, C740805:58, 1974.

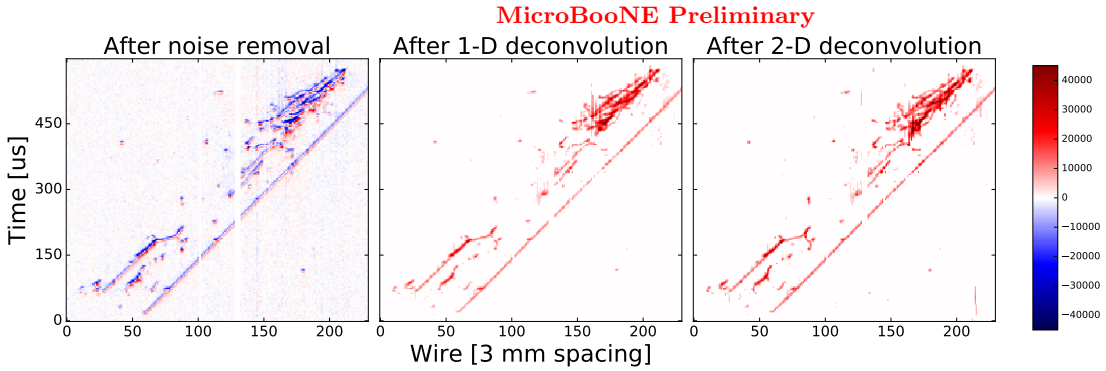

FIG. 34. 2D event display of V plane from Event 41075, Run 3493. (left) 2D view from the raw digits after the noise filtering. (middle) 2D view from the deconvoluted signal with the old 1D procedure. (right) 2D view from the deconvoluted signal with the new procedure described in this technote.

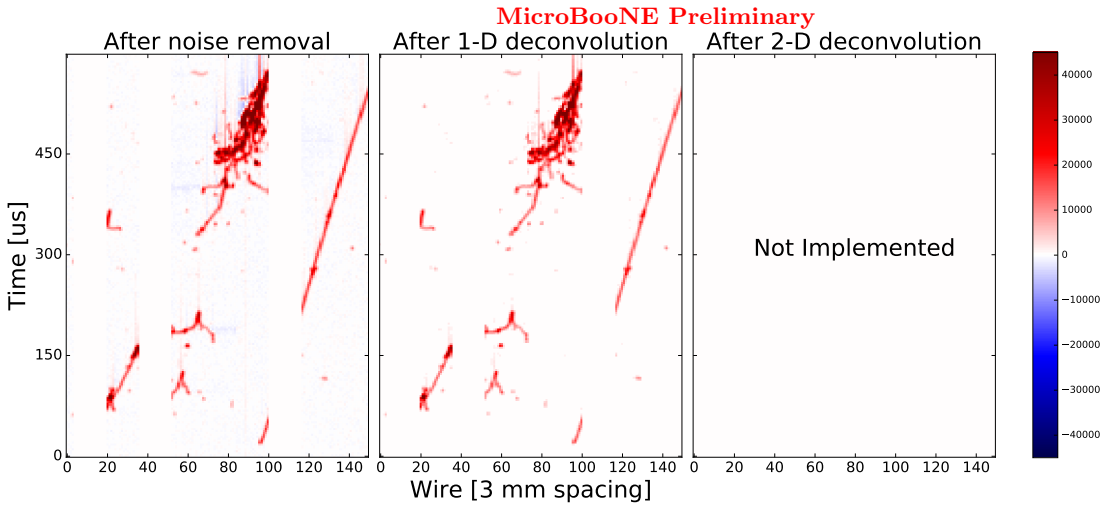

FIG. 35. 2D event display of Y plane from Event 41075, Run 3493. (left) 2D view from the raw digits after the noise filtering. (middle) 2D view from the deconvoluted signal with the old 1D procedure. (right) For collection plane, the 2D deconvolution is not necessary.

[3] H. H. Chen, P. E. Condon, B. C. Barish, and F. J. Sciulli. A Neutrino detector sensitive to rare processes. I. A Study of neutrino electron reactions. FERMILAB-PROPOSAL-0496, 1976.
[4] C. Rubbia. The liquid argon time projection chamber: A new concept for neutrino detector. CERN-EP/77-08, 1977.
[5] H. Chen et al., "Proposal for a New Experiment Using the Booster and NuMI Neutrino Beamlines: MicroBooNE," 2007. FERMILAB-PROPOSAL-0974.
[6] MicroBooNE Technical Design Report, `http://www-microboone.fnal.gov/publications/TDRCD3.pdf`.
[7] W. Shockley. Currents to conductors induced by a moving point charge. *Journal of Applied Physics*, 9:635, 1938.
[8] S. Ramo. Currents induced by electron motion. *Proceedings of the ORE*, 27:584, 1939.
[9] `http://garfield.web.cern.ch/garfield/`.
[10] J. Joshi et al., "Noise Characterization and Filtering in the MicroBooNE TPC", MicroBooNE-Note-1016-Pub.
[11] B. Baller. Liquid Argoon TPC Formation, Signal Processing, and Reconstruction (under preparation).
[12] Norbert Wiener. Extrapolation, interpolation, and smoothing of stationary time series. 1949.
[13] `http://www.phy.bnl.gov/wire-cell/`.
[14] MicroBooNE doc-db:5730 `http://microboone-docdb.fnal.gov:8080/cgi-bin/ShowDocument?docid=5730`.

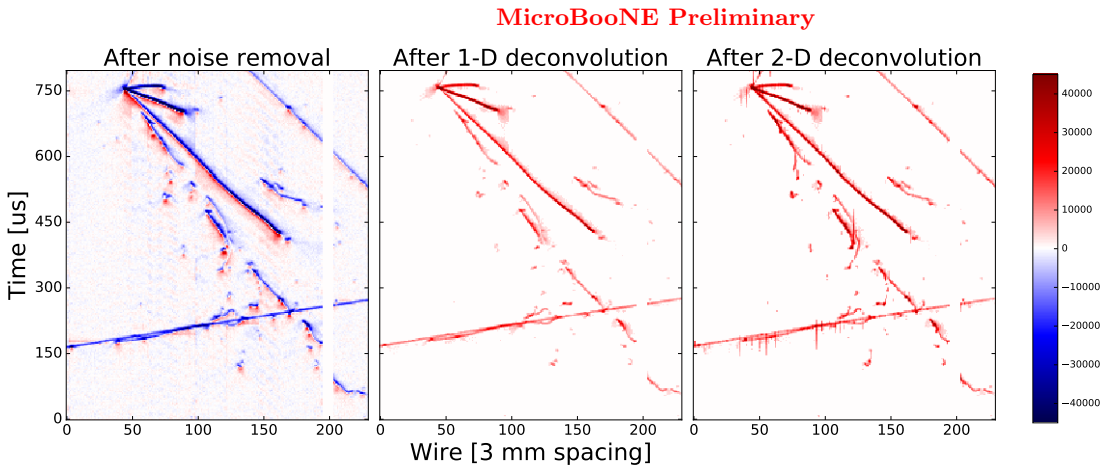

FIG. 36. 2D event display of U plane from Event 41075, Run 3493. (left) 2D view from the raw digits after the noise filtering. (middle) 2D view from the deconvoluted signal with the old 1D procedure. (right) 2D view from the deconvoluted signal with the new procedure described in this technote.

[15] Yichen Li et al. Measurement of Longitudinal Electron Diffusion in Liquid Argon. *Nucl. Instrum. Meth.*, A816:160–170, 2016.
[16] `http://lar.bnl.gov/properties/`.
[17] K.A. Olive et al. Review of Particle Physics. *Chin.Phys.*, C38:090001, 2014.
[18] `https://root.cern.ch/doc/master/classTSpectrum.html`.
[19] Technote: Reconstruction of $\pi^o \rightarrow \gamma + \gamma$ decays from muon neutrino charged current interactions in data, MicroBooNE doc-db 5864.

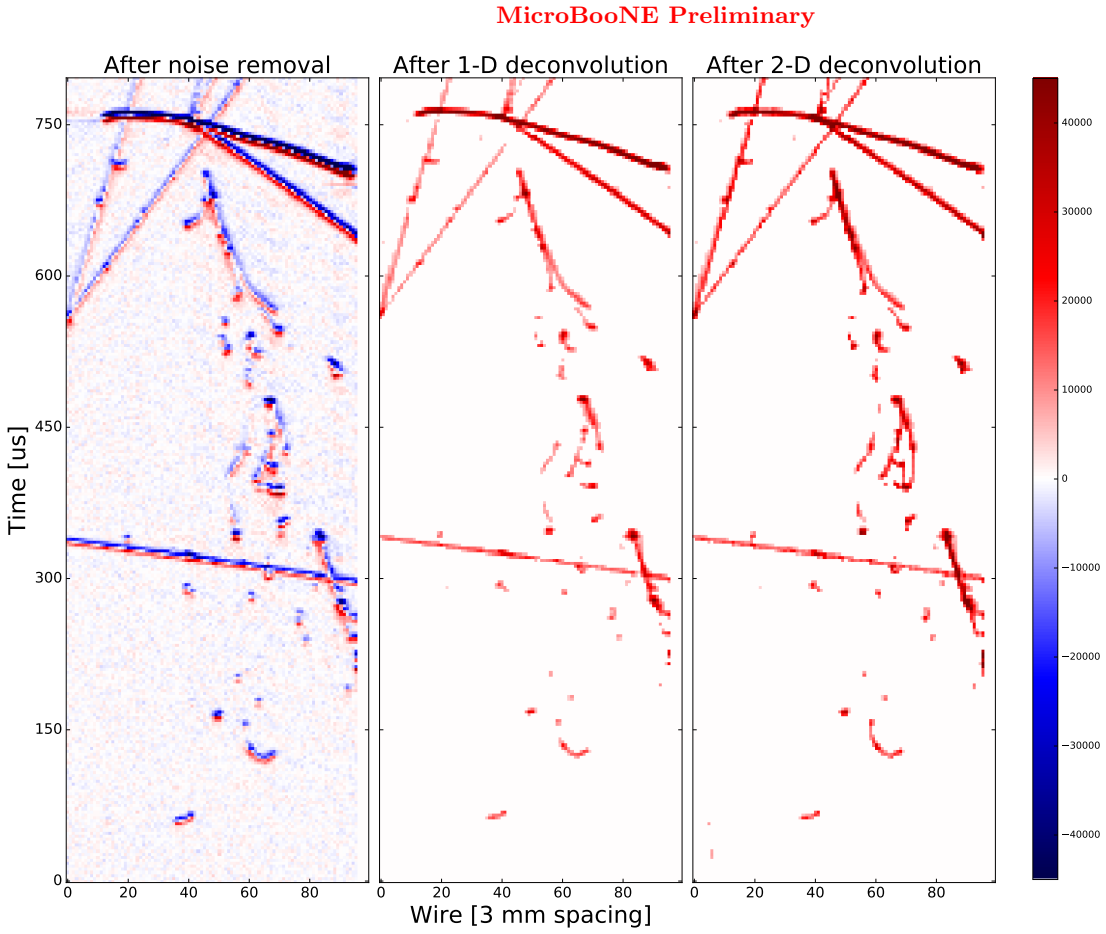

FIG. 37. 2D event display of V plane from Event 41075, Run 3493. (left) 2D view from the raw digits after the noise filtering. (middle) 2D view from the deconvoluted signal with the old 1D procedure. (right) 2D view from the deconvoluted signal with the new procedure described in this technote.

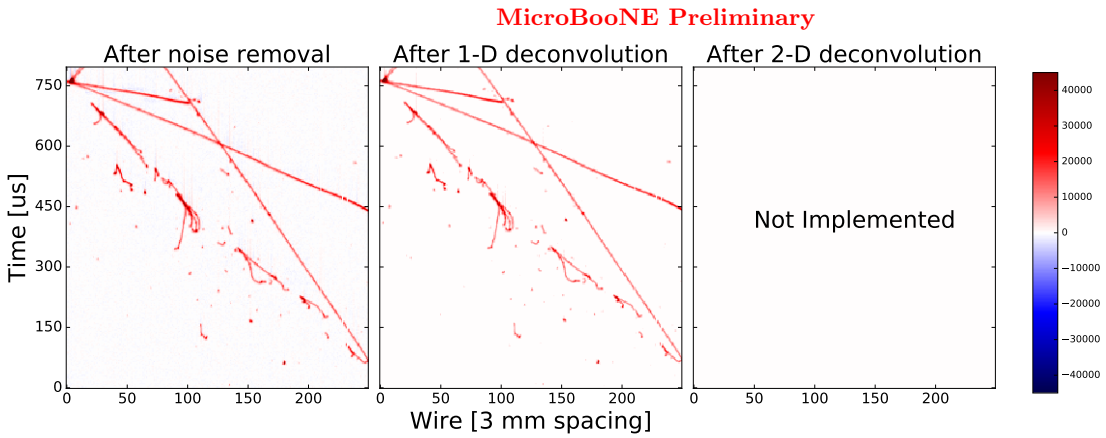

FIG. 38. 2D event display of Y plane from Event 41075, Run 3493. (left) 2D view from the raw digits after the noise filtering. (middle) 2D view from the deconvoluted signal with the old 1D procedure. (right) For collection plane, the 2D deconvolution is not necessary. The gap in the image is due to unusable channels.

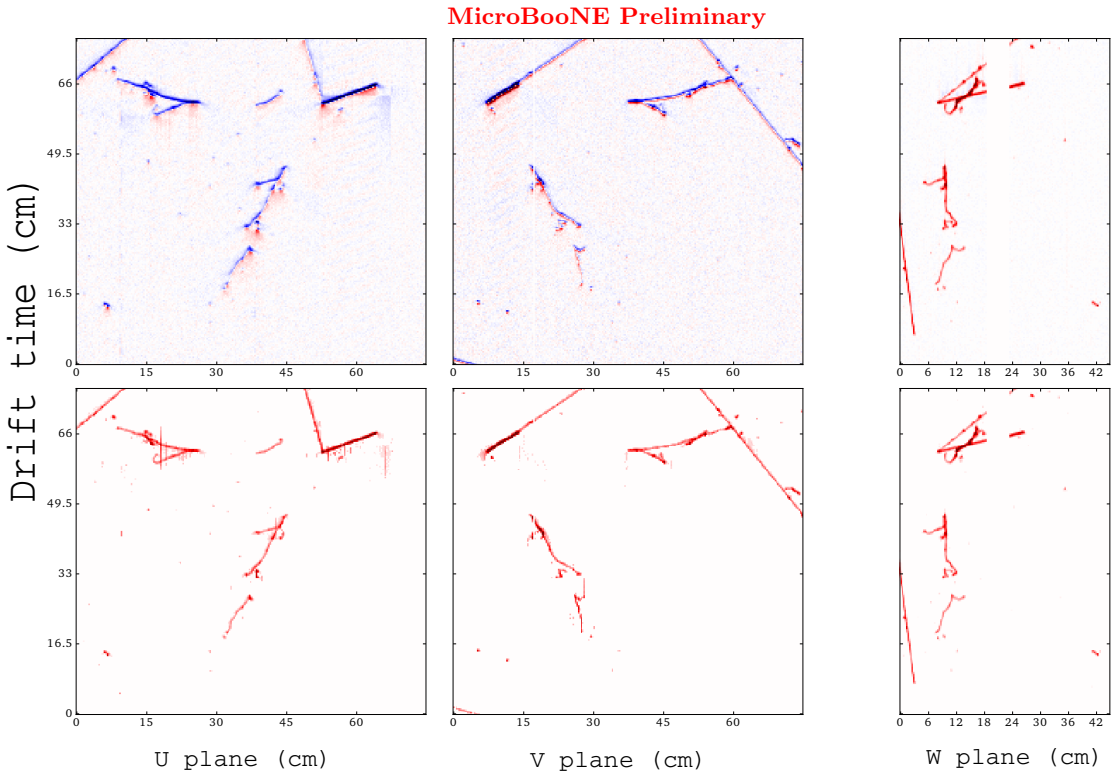

FIG. 39. Run 5975, event 4262. The top panels show the raw digits after noise filtering. The bottom panels show the extracted signal after deconvolution.

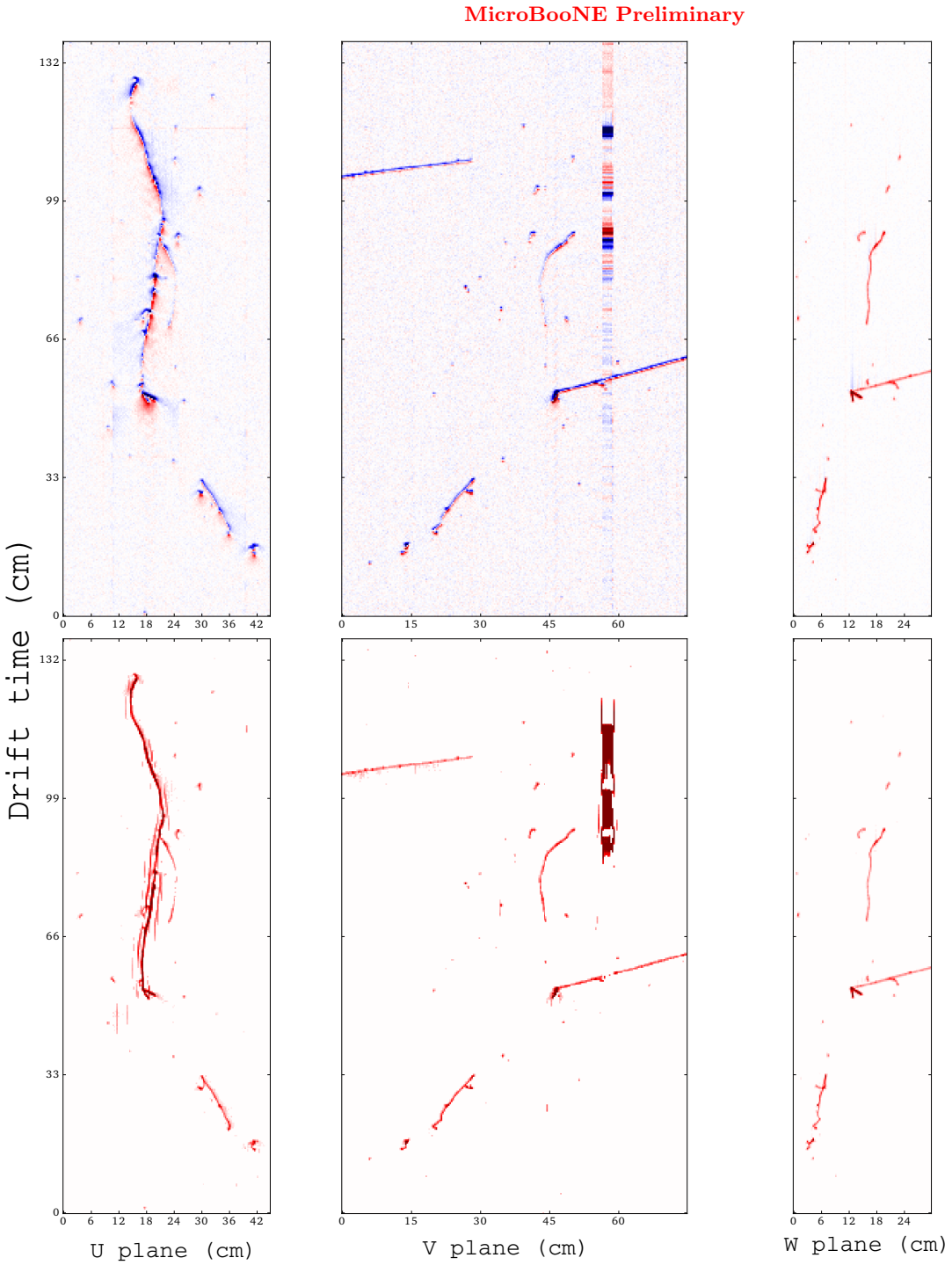

FIG. 40. Run 6058, event 8877. The top panels show the raw digits after noise filtering. The bottom panels show the extracted signal after deconvolution.

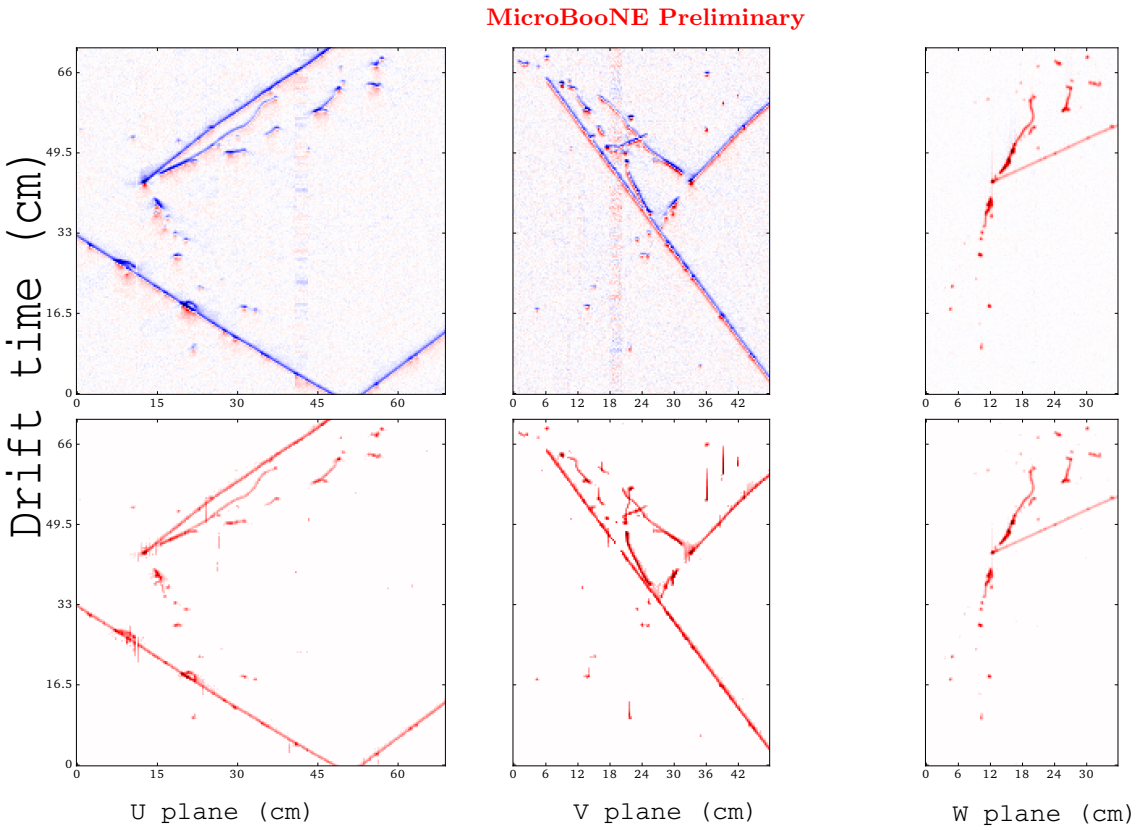

FIG. 41. Run 6058, event 4706. The top panels show the raw digits after noise filtering. The bottom panels show the extracted signal after deconvolution.

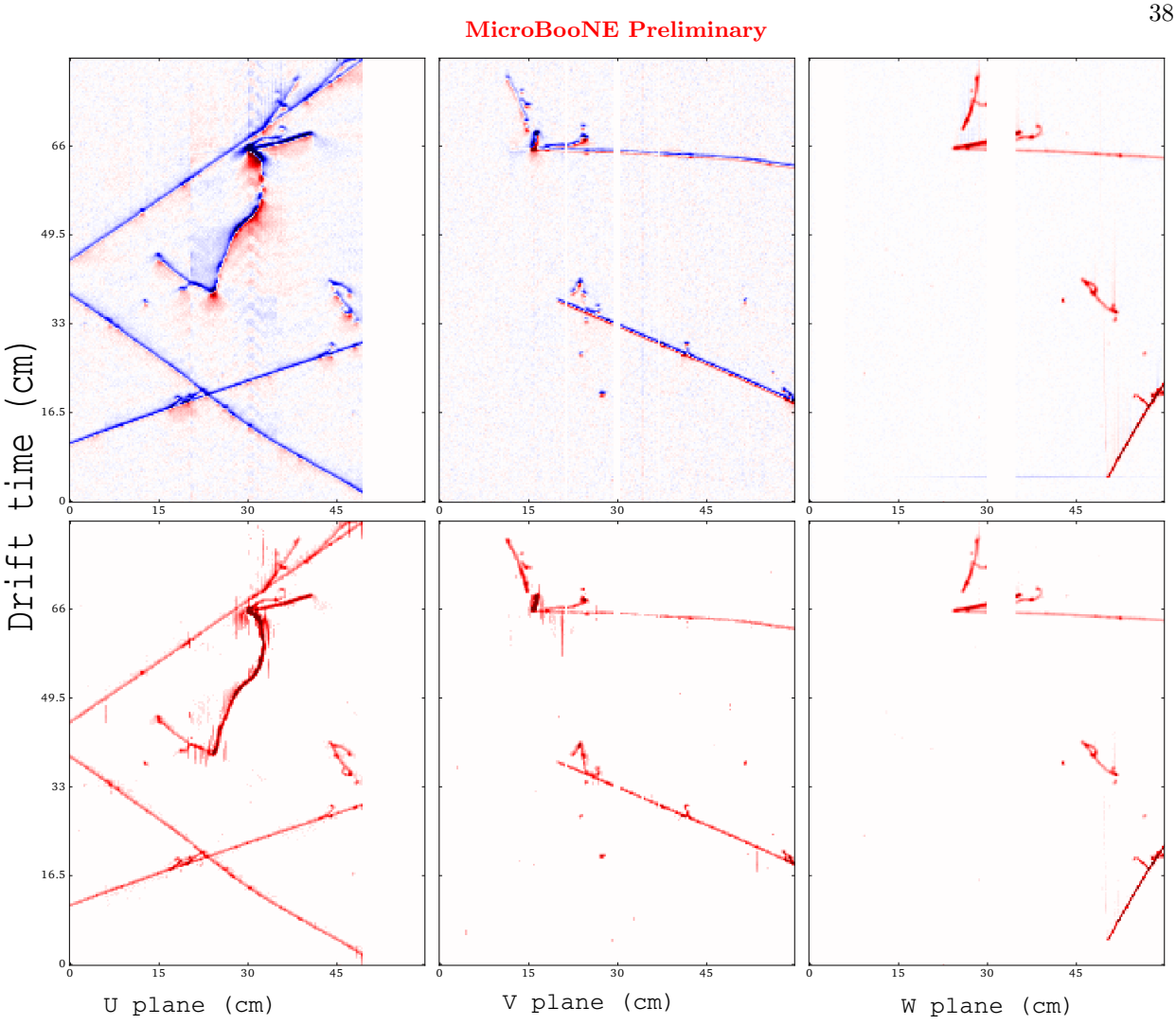

FIG. 42. Run 6145, event 814. The top panels show the raw digits after noise filtering. The bottom panels show the extracted signal after deconvolution.